The effect of irradiation on metakaolin-based geopolymer using Ti^+ ion implantation

Mahmoud A. Mahrous[1], Muhammed Abdelghany[2], Ana Carolina Constancio Trindade[3], Mohamed Aboukhatwa[4], Waltraud M. Kriven[3], Iwona Jasiuk[5*]

[1]Department of Civil and Environmental Engineering, University of Illinois at Urbana-Champaign
[2]Department of Nuclear, Plasma, and Radiological Engineering, University of Illinois at Urbana-Champaign
[3]Department of Materials Science and Engineering, University of Illinois at Urbana-Champaign
[4]Applied Research Institute, University of Illinois at Urbana-Champaign
[5]Department of Mechanical Science and Engineering, University of Illinois at Urbana-Champaign

* Corresponding author, E-mail: ijasiuk@illinois.edu

Abstract

The need for finding a replacement for concrete in nuclear power plants has increased dramatically due to concrete degradation caused by prolonged exposure to neutron irradiation. In this study, we mimicked the effect of neutron irradiation on metakaolin-based potassium geopolymer by using Ti+ as an implantation ion. Several techniques, including laser profilometry, scanning electron microscopy (SEM), backscattered electron (BSE), and nanoindentation, were employed to evaluate the geopolymer's morphological, microstructural, and mechanical properties. X-ray diffraction (XRD), Fourier-transform infrared spectroscopy (FTIR), and Raman spectroscopy were used to identify chemical composition and molecular structure before and after irradiation. Results revealed the formation of new cracks at the geopolymer surface after irradiation due to exposure to Ti+ and localized heating, accompanied by water loss and microcracking, as shown by laser profilometry. SEM and BSE analyses indicated that unreacted metakaolin disappeared, and the geopolymer microstructure became denser after irradiation. The results from nanoindentation showed a 90% increase in microhardness, a 46% increase in the reduced modulus, and a 23% reduction in the contact depth after irradiation. The FTIR spectra demonstrated a reduction in the intensity of O-H stretching vibration and H-O-H peaks after irradiation. XRD patterns indicated no changes in the geopolymer structure following irradiation. However, Raman spectroscopy revealed a decline in intensity, peak shift, and an increase in full-width half maximum (FWHM) after irradiation, likely attributed to the presence of titanium ions in the target and the thermal shock due to the irradiation. The increase in FWHM suggests increased sample disorder and alterations in bond angles, bond distance, or the local environment. This research is crucial for developing eco-friendly and resilient nuclear reactor shielding materials using geopolymers.

Keywords: *Ion beam irradiation, Metakaolin-based potassium geopolymer, radioactive waste, nanoindentation, FTIR, Raman spectroscopy, XRD.*

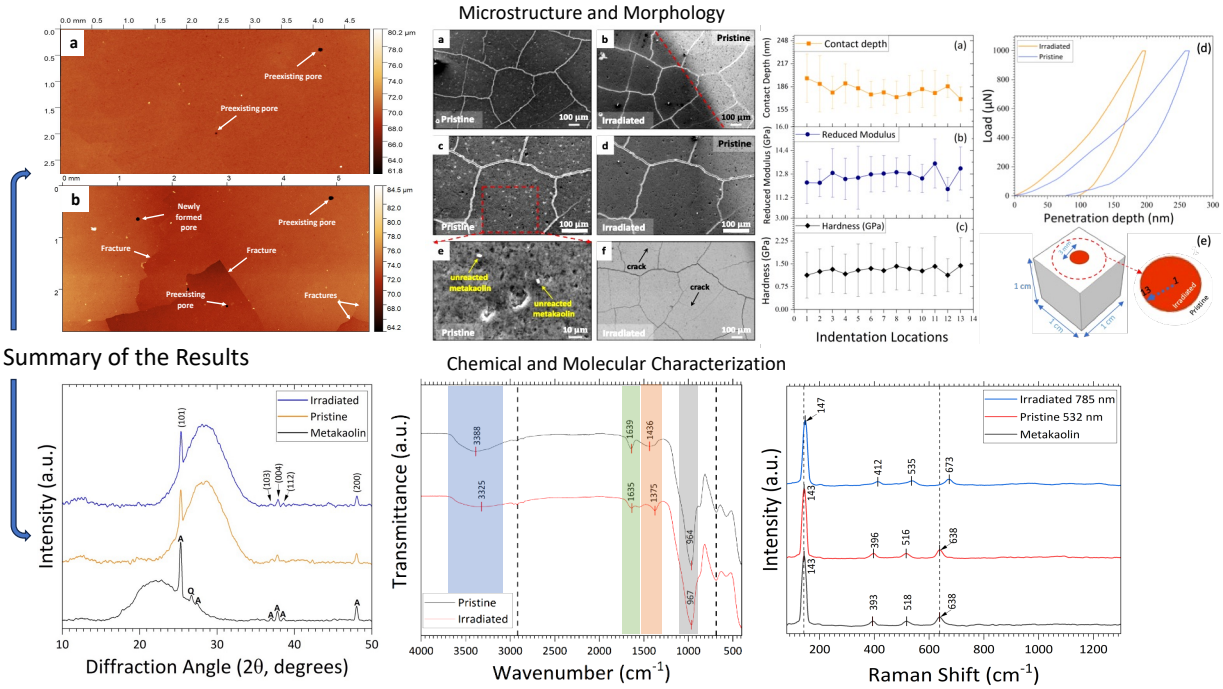

1 Introduction

Nuclear power plants (NPPs), particularly commercial light water reactor (LWR) buildings, which include safety-related structures such as containment and biological shielding buildings, are predominantly constructed with concrete [1]. Concrete degrades during its lifetime by prolonged exposure to neutron irradiation. The effect of irradiation on concrete has been well-studied and documented [2–5]. Generally, the performance of concrete (e.g., mechanical properties) in NPPs is acceptable for the first 40 years of service life. Then, it declines significantly even with lower neutron fluence values (E > 0.1 MeV) [6]. Concrete is a complex material comprising fine and coarse aggregates, water, and cement paste. One of the most common degradation mechanisms in concrete structures is the alkali-silica reaction (ASR), which occurs due to the reaction between the alkaline solution and the silica-rich aggregates (e.g., silicate-based minerals). ASR develops an alkali-silica gel that swells in the presence of moisture and, consequently, forms a map-like crack in the concrete structure [7]. Additionally, cement paste consists of amorphous calcium silicate hydrate (C-S-H) gel, which has a highly porous structure with about 20% pore volume [8]. As a result, the effect of neutron irradiation on cement paste is believed to be much smaller compared to the minerals and aggregates and typically results in cement paste shrinkage. The reason is that the threshold energy required for neutrons to cause damage to the cement paste is relatively high, around 0.8 MeV [8]. It has been reported that ion beam irradiation significantly influences producing ASR within the concrete microstructure due to a transition from a crystalline to an amorphous state [9]. Therefore, ASR is considered a severe threat to NPPs structures. On the other hand, Yang *et al.* [10] investigated the effects of alkali-silica reaction (ASR) on the pore distribution in fly ash geopolymer concrete. They compared it to ordinary Portland cement concrete using microcomputed tomography (Micro-CT) and showed that ASR is less severe in fly ash geopolymer concrete than in Portland cement concrete. Thus, there is a pressing need to study the effect of irradiation on geopolymer paste which could be a potential replacement for cement paste for NPPs.

Geopolymers are inorganic polymeric, ceramic-like structures formed through the reaction between an aluminosilicate source (e.g., metakaolin, fly ash, red mud) and an alkali-rich solution (activator) at room temperature [11–13]. Geopolymers have emerged as an eco-friendly alternative to conventional construction materials like concrete due to their exceptional mechanical properties [14–17] and fire resistance [18]. These attributes have opened exciting opportunities for the application of geopolymers, including as a replacement for Portland cement [19], fire-resistant materials [20,21], and environmental applications, including waste immobilization [22–24], soil stabilization [25,26], and nuclear waste management [27–30].

Several studies reported on the effect of gamma rays on geopolymers, but there is limited research on the effects of neutron and ion irradiation on these materials. Lambertin *et al.* [31] investigated the effect of radioactive waste on geopolymers by studying the impact of gamma-ray irradiation on metakaolin-based sodium geopolymers. They concluded that irradiation led to changes in pore size distribution and structural relaxation caused by the reorganization of thin pore walls under the influence of radiation. Additionally, Deng *et al.* [32] studied the leaching of 133Cs+ radionuclides from geopolymer waste forms by exposing them to gamma-ray irradiation. Their results indicated that gamma-ray exposure did not alter the morphology of the geopolymers but did change their pore size distribution. Consequently, geopolymers have the potential to replace concrete as radiation shielding materials in nuclear reactors. However, the effects of ion radiation on the microstructure, mechanical and chemical properties, and stability of geopolymers, need to be investigated.

Thus, this paper addresses the effects of ion beam irradiation, which mimics the nuclear reactor environment, on metakaolin-based potassium geopolymer. This research aimed to evaluate changes in the surface topology, mechanical properties, and chemical bonding and vibrational mode of molecules of a geopolymer before and after irradiation. A laser profilometer, scanning electron microscopy (SEM), and backscattered electrons (BSE) were employed to assess the microstructure, while nanoindentation was used to measure the mechanical behavior of geopolymers before and after irradiation. X-ray diffraction (XRD), Fourier-transform infrared spectroscopy (FTIR), and Raman spectroscopy were employed to detect alterations in the geopolymer's crystallographic, chemical, and molecular structures after irradiation.

Understanding the effect of irradiation on geopolymers is needed for developing robust, safe, and sustainable nuclear reactor shielding materials. Moreover, this research should lead to the development of radiation-resistant geopolymer materials that are better suited for use in high-radiation environments such as nuclear waste containers, space shuttles, and satellites. Also, using geopolymers provides environmental benefits as they are usually produced from industrial waste materials, like fly ash and slag, which helps reduce waste in landfills. Additionally, amorphous geopolymers do not undergo the same crystalline-to-amorphous structure transition as cement. Thus, using geopolymers could mitigate the risk of ASR and alkali-carbonate reaction (ACR) in the presence of radiation exposure which is common in concrete.

This paper is divided into five sections. Section 2 describes the geopolymer synthesis and methods. Section 3 presents the results. Section 4 demonstrates the discussion. Section 5 contains the conclusions and extensions of the work.

2 Materials and Methods

2.1 Geopolymer Synthesis

The main geopolymer compounds were manufactured following a well-established mix design employed in other studies [33]

$K_2O•2SiO_2•11H_2O + 2SiO_2•Al_2O_3 \rightarrow K_2O•Al_2O_3•4SiO_2•11H_2O$.

The alkali solution ($K_2O•2SiO_2•11H_2O$), also known as a water glass (WG), was prepared by dissolving 90% pure potassium hydroxide pellets (Sigma-Aldrich, St. Louis, MO) in deionized water using a magnetic stirrer, with the subsequent addition of fumed silica (Cab-o-sil Cabot Corp., Boston, MA, USA). The solution was kept on the stirrer at medium speed for 24 hours and then placed in a controlled temperature environment up to 5 ºC before its use.

The geopolymer paste was prepared by combining WG with a highly reactive metakaolin (MK) (Metamax, BASF Corp., Florham Park, NJ, USA), with a WG/MK ratio of 1.85. Metamax metakaolin powder chemical composition was determined using the Shimadzu EDX-700 instrument and is presented in Table 1. Both components were added to a plastic becker and shear mixed under a high torque condition set at 400 rpm for 1 minute, followed by high speed at 2000 rpm for 9 minutes. Next, the mixture was put into a Thinky ARE-250 planetary conditioning mixer (Intertronics, Kidlington, Oxfordshire, UK), which ran at 1200 rpm for 30 seconds and 1400 rpm for another 30 seconds to mix the components thoroughly and avoid air bubbles in the geopolymer. The fresh mix was subsequently poured into a silicone mold with cubic spaces of $10\ mm \times 10\ mm \times 10\ mm$ while placed on a vibrating table (FMC Technologies, Houston, TX, USA) to remove the trapped air bubbles which were introduced in the previous step. The mold was covered with a plastic sheet and kept at 50 ºC for 24 h for thermal curing to guarantee proper reactivity before demolding. A subsequent curing period of 7 days was conducted at room temperature conditions.

Table 1. Chemical composition of metakaolin powder, all values are in wt%.

Material Type	SiO_2	Al_2O_3	TiO_2	Fe_2O_3	K_2O	SO_3	V_2O_5	CuO
Metakaolin	52.3	44.9	1.92	0.53	0.09	0.7	0.06	0.04

2.2 Sample preparation and ion-irradiation

Before the ion-irradiation, the samples were cold-mounted in conductive mounts (epoxy resin + Ni powder). They were mechanically ground and polished using a Struers Tegramin-25 automatic polisher. Grinding was performed on an MD-Piano 220 grinding surface, while polishing was carried out using an MD-Plan cloth with 9 µm diamond suspension. Final polishing was performed on an MD-Chem cloth with 0.25 µm fumed silica. A polished metakaolin-based geopolymer sample with a dimension of $1\ cm \times 1\ cm \times 1\ cm$ was used for laser profilometry, SEM, BSE, nanoindentation, FTIR, and Raman spectroscopy. The sample was grounded using a pestle and mortar until a fine homogeneous powder was obtained for XRD testing following irradiation.

Since there is no prior literature on the effect of ion radiation on geopolymer and most of the work has been done using gamma X-ray, it was difficult to specify the necessary dose of ion irradiation to induce the damage expected in a typical nuclear

reactor environment. Thus, the ion fluence was chosen to produce similar damage occurring in concrete, the most common construction material used in nuclear power plants. However, we choose the ion fluence based on the amount of ion irradiation that can induce the same damage that neutron irradiation can cause to the concrete after 40 years of operation of the nuclear reactor. Field *et al.*[34] reported that a fluence level where the deleterious effect of irradiation on concrete was observed after more than 40 years of nuclear power plant operation is near 10^{19} n/cm^2. Typically, the energy deposition rate of ion bombardments is about 10^5 times more than the corresponding neutrons bombardment [35]. Therefore, the ion beam fluence has to be greater than 10^{14} cm^{-2}. In our case, the samples were irradiated using a 3SDH Pelletron accelerator (National Electrostatics Corporation (NEC), Middleton, Wisconsin, USA) at ambient temperature using a 526 keV Ti^+ ion beam to a fluence of 10^{16} cm^{-2} using an average beam current of 24 nA for 43 minutes exposure duration. The ion beam was created in a source of negative ions by cesium sputtering (SNICS) using a titanium hydride cathode.

The SRIM (Stopping and Range of Ions in Matter) Monte Carlo Binary Collision Approximation (BCA) software [36] was used to simulate the Ti^+ irradiation process of the [32] geopolymer. In this simulation, a 10^5 Ti^+ ions with an energy of 526 keV bombarded the target surface at normal incidence. The target was modeled as a 3-Dimensional amorphous system composed of Si-Al-K-H-O (following the geopolymer chemical formula $K_2O•Al_2O_3•4SiO_2•11H_2O$) with 1.704 g/cm^3 density and thickness of 3 µm. We calculated the implantation profile of the incident ions as a function of the target depth, as shown in Figure 1. The y-axis represents the percentage of the incident ions implanted, and the x-axis indicates the depth penetrated by the ions in the target. The radiation range of Ti^+ in the geopolymer was found to be around 623 nm.

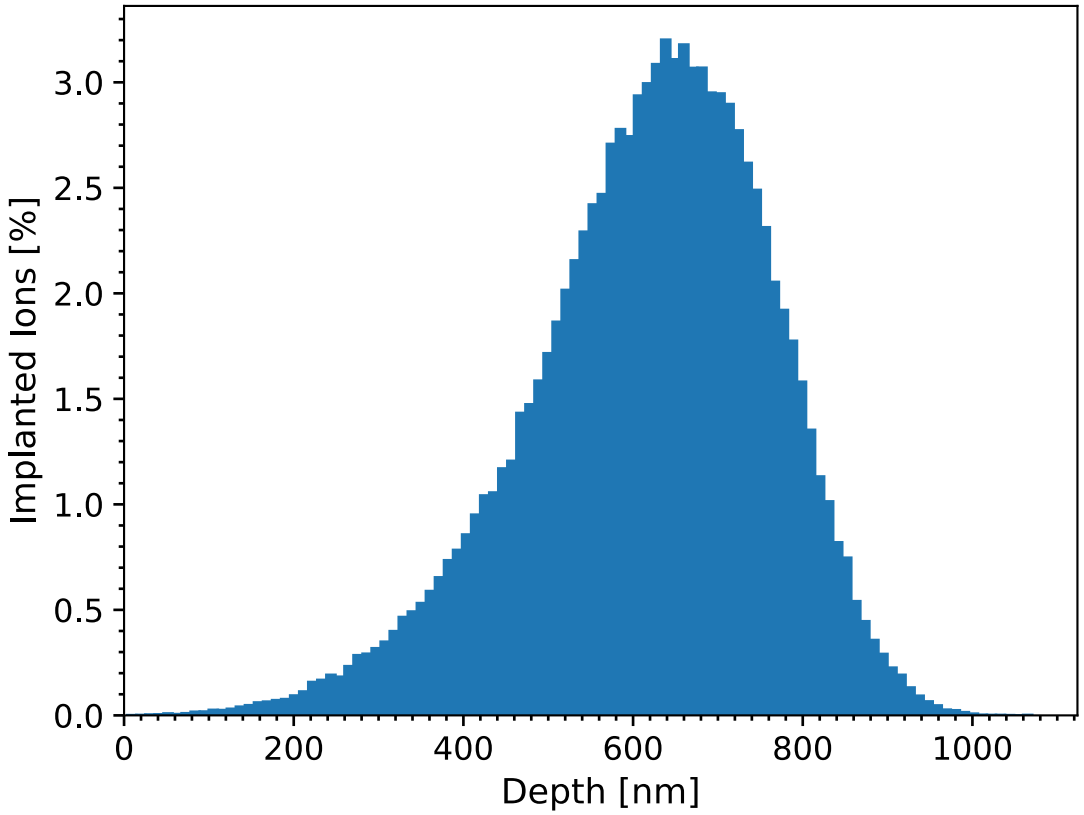

Figure 1. Implantation profile of Ti^+ ions as a function of depth due to 526 keV Ti^+ irradiation of geopolymer target at normal incidence as calculated using SRIM.

2.3 Laser Profilometry

Surface topography measurements were performed using Keyence VK-1000 3D laser scanning confocal microscopy (Keyence Corporation, Osaka, Japan) to study the topographic changes of the sample surface after irradiation. The measurements were done before and after ion irradiation using 20x magnification. These 3D surface topography images giving height maps were processed using Gwyddion software [37].

2.4 Scanning Electron Microscopy (SEM) and Backscattered Electron (BSE)

The morphological and microstructural study was performed using environmental scanning electron microscope FEI Quanta™ FEG 450 ESEM (FEI Company, Hillsboro, Oregon, USA). The instrument was equipped with Robinson series 6 scintillator-type backscattered electron detector (BSD) and solid-state low- and standard voltage BSDs. SEM imaging was carried out at various magnifications with an accelerating voltage of 20 kV. BSE imaging was conducted with an accelerating voltage of 10 kV. Since the sample was embedded in a conductive epoxy mount to discharge the electric charge produced during the irradiation and SEM scanning, no sputtering was required.

2.5 Nanoindentation

Mechanical properties of the specimen before and after irradiation were determined using Hysitron nanoindenter TI 950 with an upgraded controller using XPM accelerated property mapping function (Bruker Corporation, Billerica, MA, USA). One hundred indents were performed over an area of $60 \times 60\ \mu m^2$, with a fixed maximum load of 1 mN for pristine and irradiated samples. For the pristine sample, a total of three indentations were conducted at three different locations within the center of the sample. Additionally, thirteen indentations were performed on an irradiated sample, starting from the center of the irradiated region and extending outward toward the border between the irradiated and pristine area, as illustrated in the diagram in Figure 5(e). The separation distance between the first 10 indents was 100 μm, and for the remaining three indentations, it was 500 μm. The separation distances and the maximum load were carefully selected to prevent interaction between the indents for pristine and irradiated samples.

Young's modulus was calculated using the following equation [38]

$$E = (1 - \nu^2)\left[\frac{1}{E_r} - \frac{1 - {\nu_i}^2}{E_i}\right] \quad (1)$$

where ν is the Poisson's ratio of the geopolymer, which is assumed to be 0.3 as suggested by Chen *et al.* [39], E_r is the reduced elastic modulus, E_i and ν_i are the Young's modulus and Poisson's ratio of the indenter, which are 1140 GPa and 0.07 for diamond, respectively [38].

2.6 X-ray Powder Diffraction (XRD)

XRD analysis was conducted on metakaolin and geopolymer samples in powdered form and an irradiated geopolymer in solid form. The solid irradiated sample was a flat, finely polished disc with a thickness of 1 cm. The analysis was performed using a Bruker D-8 Discover diffractometer (Bruker, Billerica, MA, USA) equipped with a copper X-ray source (CuKα, λ= 1.544 Å) operated at 40 kV and 40 mA, with a step size

of 0.01° and a scan rate of 0.5 steps/s. The diffraction pattern was collected over a 2θ range of 10-50°. The resulting diffraction pattern was analyzed using the Jade software package to identify each phase present in the sample. The software was calibrated using the ICSD database to ensure accurate phase identification.

2.7 Fourier-transform Infrared Spectroscopy (FTIR) and Raman Spectroscopy

FTIR and Raman spectroscopies were utilized to analyze the chemical composition and molecular structure of the metakaolin-based geopolymer before and after irradiation. The FTIR analysis was carried out using a Perkin-Elmer Spectrum One (PerkinElmer, Shelton, CT, USA) FTIR Frontier spectrometer with a universal attenuated, total reflection (UATR) polarization tool. To ensure optimal contact and generation of internal reflection during the FTIR analysis, a polished surface was pressed against a diamond crystal with a force of 85 N. FTIR spectra were collected in the range of 4000-400 cm^{-1} with a spectral resolution of 4 cm^{-1} on both pristine and irradiated samples. The FTIR scans were conducted on a total of three different irradiated samples and one pristine sample at four different points within each irradiated sample and at four different locations within the pristine sample. The spectra presented in this study are the average of 12 scans for the irradiated samples and four scans for the pristine sample. Raman spectra were obtained using a Confocal Raman microscope Raman 11 (Nanophoton, Osaka, Japan) with a 532 nm and 785 nm excitation laser. Raman spectra were collected on a powdered metakaolin and pristine geopolymer sample using a laser with a 532 nm wavelength and a grating of 1200 gr/mm. For the solid irradiated sample, a 785 nm wavelength laser was used. Raman spectra were collected using a 20x objective lens and a slit width of 50 μm over an area of 15 μm × 15 μm with an exposure time of 10 s, and a total of 301,550 points were collected in each scan. The spectra were collected in the range of 70-1300 cm^{-1} with a peak position accuracy of 0.1 cm^{-1} and a spectral resolution (FWHM) of 1.6 cm^{-1}.

3 Results

3.1 Microstructure and Morphology Analysis

3.1.1 Laser Profilometry

Figure 2 shows the laser profilometry scans illustrating the surface topology of the metakaolin-based geopolymer before and after irradiation. The sample topography before irradiation (pristine) has a smooth crack-free surface (Figure 2(a)). However, after irradiation, a noticeable crack formed in the center and another in the corner of the area exposed to radiation (Figure 2(b)). After irradiation, the geopolymer surface exhibits the formation of new pores, as shown in Figure 2(b). This phenomenon is attributed to the irradiation-induced temperature increase leading to localized expansion and vaporization of entrapped moisture within the specimen. The newly formed cracks and pores contribute to changes in the surface topography and can impact the material's mechanical and thermal properties. Figure 2(c) shows the line profiles (A-B) of the geopolymer surface before and after irradiation. The line profile across the sample surface before irradiation exhibits minimal changes in surface roughness. In contrast, the line profile following irradiation drops significantly with a sharp peak at the location of the newly formed crack. This drop could be attributed to the shrinkage caused by the evaporation of bound water resulting from localized heating, thermal shock, and Ti^{+} deposition. Generally, irradiation modified the surface due to the formation of new cracks and pores and the surface shrinkage observed from the line profile.

3.1.2 Scanning Electron Microscopy (SEM) and Backscattered Electron (BSE)

The microstructure and the morphology of the geopolymer specimens were analyzed using SEM and BSE imaging techniques. Figure 3 displays SEM and BSE images of the geopolymer microstructure at different magnifications, taken at the same position, before and after irradiation. Figure 3(a) shows a map-like crack formation on the geopolymer surface. The red line drawn in Figure 3(b) indicates the boundary between the pristine and irradiated geopolymer sample surfaces. Following irradiation, the surface of the geopolymer exhibits a darker color compared to the pristine condition, as indicated by the red line drawn between the pristine and irradiated areas on the sample surface in Figure 3(b). The backscattered electron (BSE) technique was utilized in this study to examine the surface morphology and assess the penetration depth of the irradiation effect within the sample. Figure 3(f) is a BSE image of the geopolymer surface after irradiation. There is no color difference between the pristine and irradiated areas, like what was observed in the SEM image. Additionally, the observation from the SEM image, as well as the BSE image (Figure 3(f)), indicated that the effect of irradiation was primarily confined to the immediate vicinity of the sample surface. No discernible color difference was observed between the pristine and irradiated areas in the BSE image, further confirming the shallow depth of the irradiation effect, as detected by both SEM and BSE techniques. Furthermore, the surface cracks depicted in Figure 3(f) are more noticeable (shown by the red arrows) when compared to the SEM image displayed in Figure 3(a). The magnified area of the pristine sample in Figure 3(e) shows that the sample had many voids containing unreacted metakaolin powder. In contrast, following irradiation, the same area exhibited a more uniform and compact microstructure characterized by the absence of unreacted metakaolin particles. This phenomenon can be attributed to the temperature increase caused by Ti+ bombardment, as the energy from radiation is converted into heat [40]. Figure 4 displays SEM and BSE images comparing a pristine sample to an irradiated sample. In Figure 4(a), the pristine sample exhibits no noticeable cracks near the prominent diagonal crack (highlighted by a red arrow). However, following irradiation, a significant crack becomes apparent in Figures 4(b) and 4(c), originating from the pre-existing crack at the same location prior to irradiation. Furthermore, an additional crack emerges (indicated by yellow arrows) in Figures 4(b), 4(c), and 4(d). Furthermore, the newly formed cracks after irradiation are clearly indicating that a potential increase in sample vulnerability to mechanical stress after exposure to ionizing radiation.

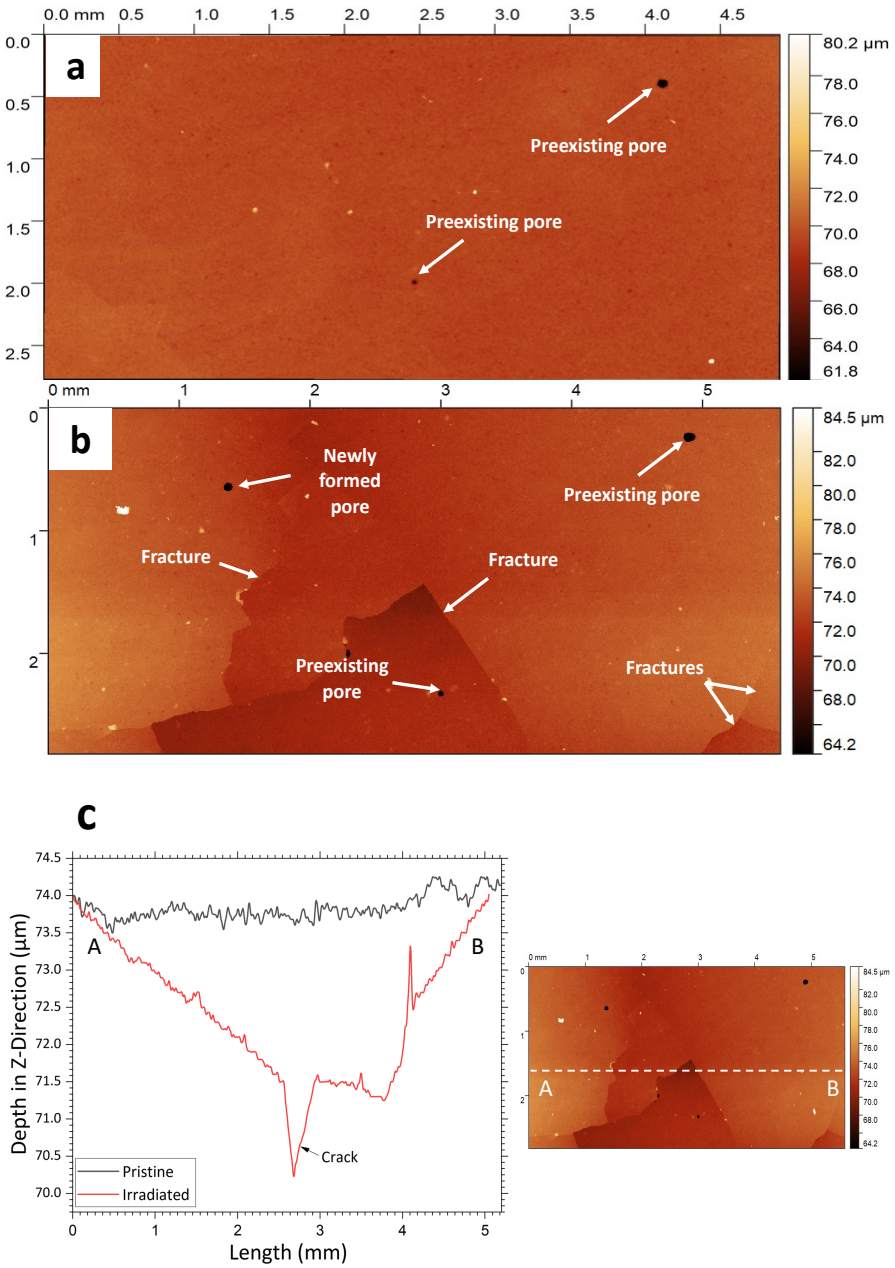

Figure 2. Height change map obtained using a laser profilometer for a metakaolin-based geopolymer sample before and after irradiation: (a) the height map of the sample in its pristine condition, (b) the height map after irradiation, and (c) the line profile representing the change in height topography of a pristine and an irradiated sample.

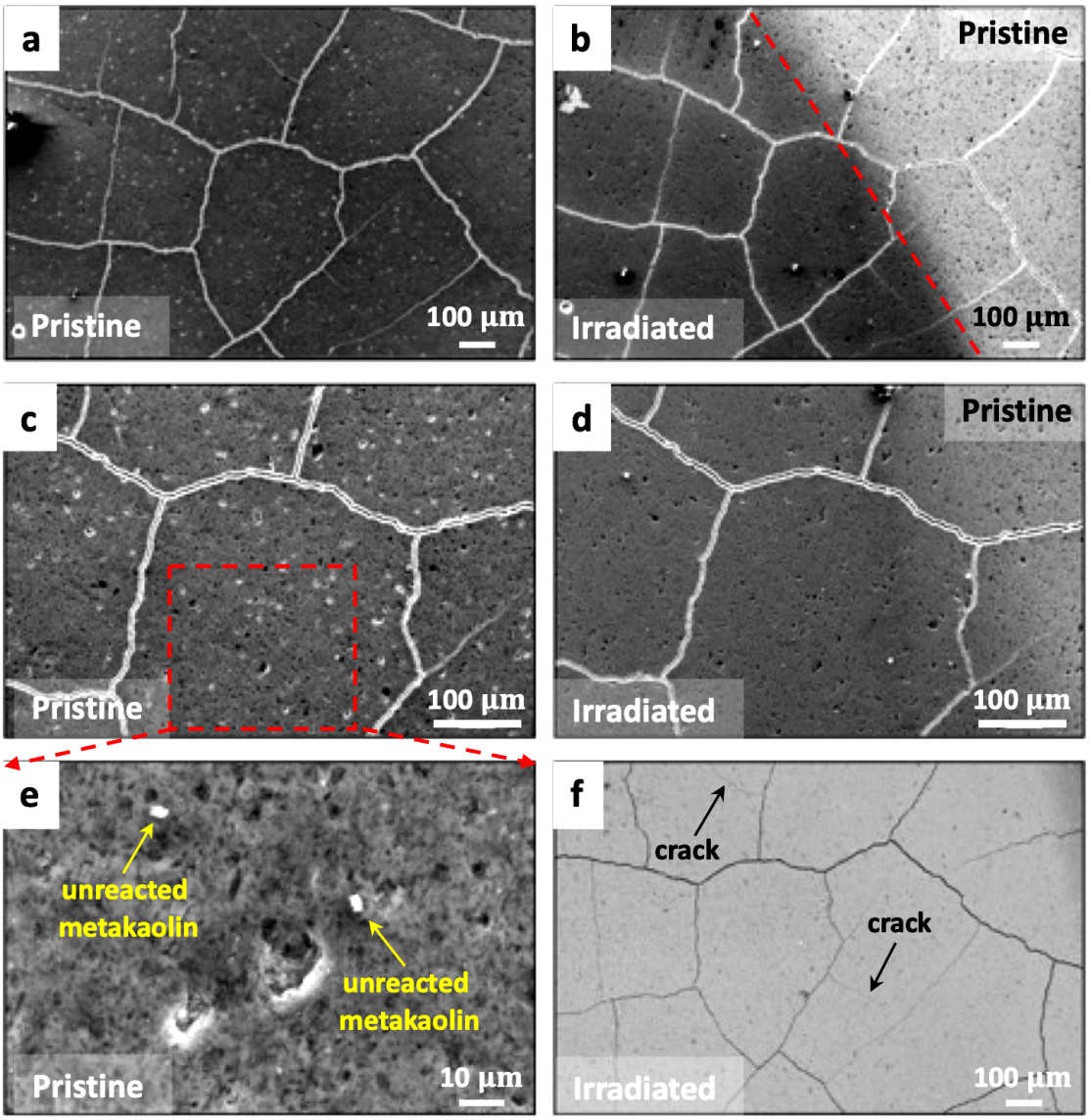

Figure 1. Scanning electron microscopy (SEM) and backscattered electron (BSE) images at different magnification for metakaolin-based geopolymer before and following irradiation. (a) SEM image at pristine (original) condition, (b) SEM image following irradiation, with a red line indicating the boundary between the pristine and irradiated regions, (c) pristine SEM image at 240x, d) irradiated SEM image at 240x, and e) pristine SEM image at 2130x. f) BSE image following irradiation.

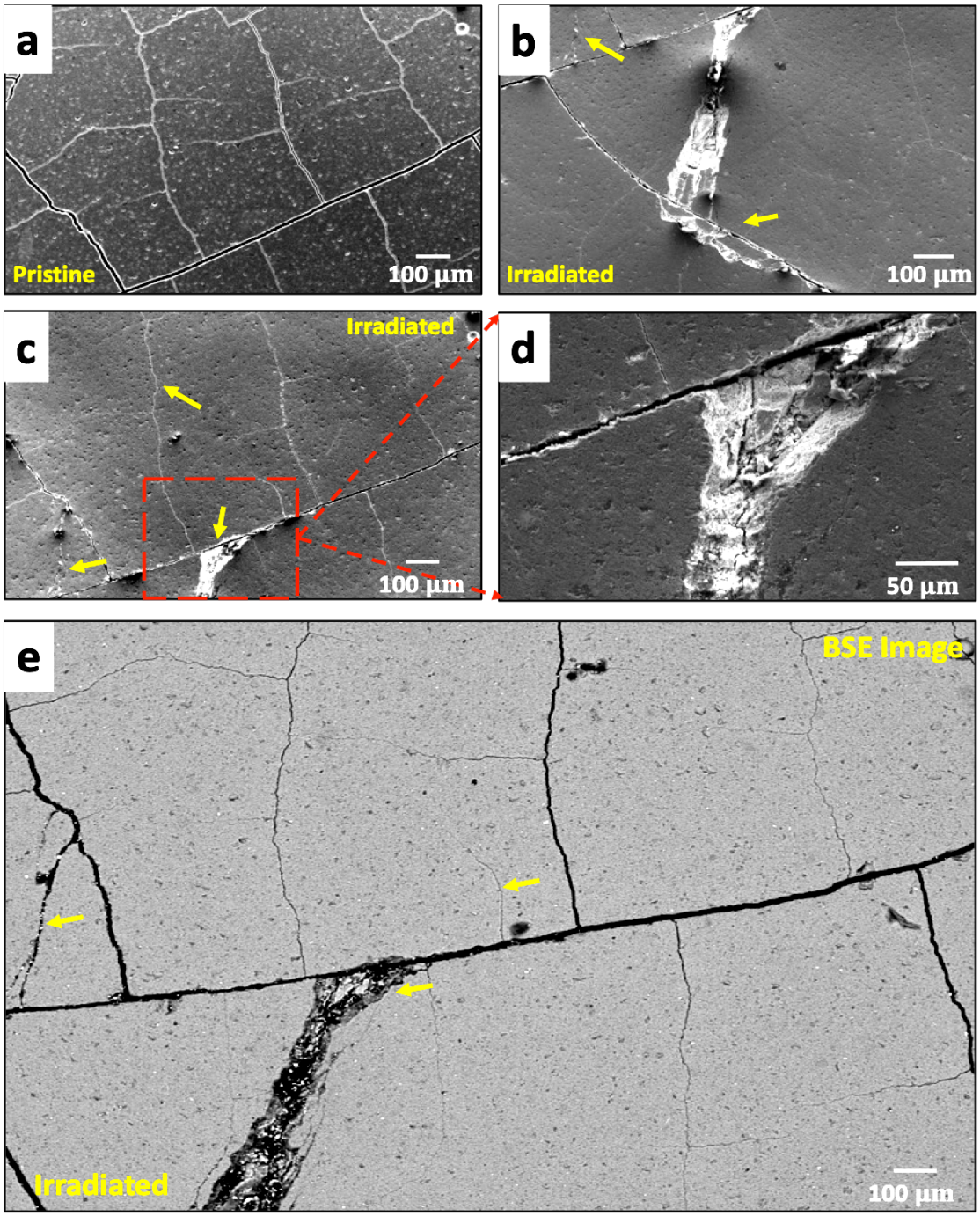

Figure 2. Scanning electron microscopy (SEM) and backscattered electron (BSE) images at different magnifications for metakaolin-based geopolymer, before and after irradiation. (a) SEM image at pristine condition, (b) SEM image for the irradiated condition; yellow arrows are showing the newly formed cracks after irradiation, (c) irradiated SEM image, (d) SEM image of the crack for irradiated the sample at 600x, and (e) BSE image following irradiation with yellow arrows indicating the newly formed cracks.

3.1.3 Nanoindentation

Nanoindentation is an essential tool used to understand the nano/micromechanical properties of materials. In this study, we utilized nanoindentation to investigate the microscale mechanical properties of geopolymers before and after irradiation. Figures 5(a), (b), and (c) depict the contact depth, reduced modulus, and microhardness, respectively, obtained from 13 different locations in the sample. The measurements began at the center of the irradiated area and were repeated in an outward direction towards the pristine area of the sample, as illustrated in Figure 5e. The nanoindentation mechanical properties of pristine and irradiated geopolymer samples are summarized in Table 2.

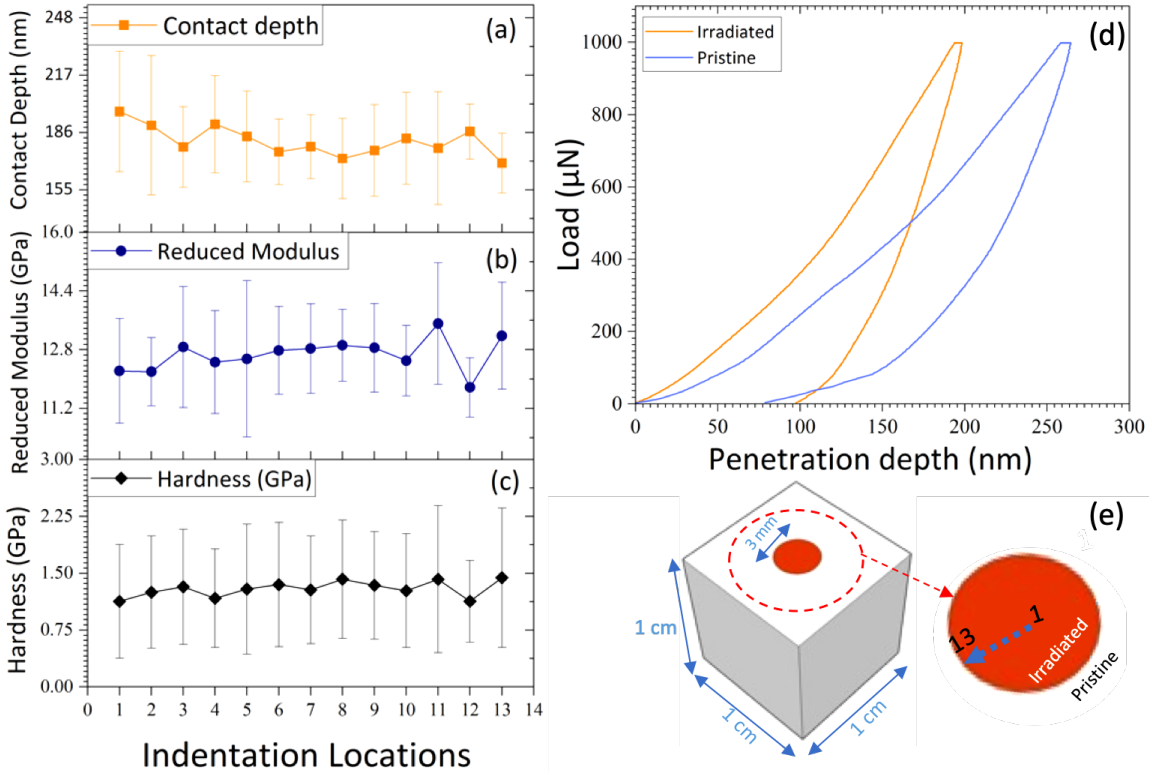

Figure 4. Results of nanoindentation tests conducted on pristine and irradiated metakaolin-based geopolymer. (a), (b), and (c) are the nanoindentation results of contact depth, reduced modulus, and microhardness for 13 different locations (with location 1 being at the center of the irradiated area and location 13 being at the outermost location of the irradiated area), (d) the load versus displacement plot for both pristine and irradiated metakaolin-based geopolymer, and (e) schematic representation for the nanoindentation locations on the irradiated sample, where number 1 is in the center of the ion beam and location 13 is the most outer point towards the pristine part of the sample.

The average nanoindentation results obtained from the pristine and irradiated samples are reported in Table 3. The results show that the average microhardness, Young's modulus, reduced modulus, and contact depth for the irradiated sample are 1.29 ±0.10 GPa, 11.77 ±0.56 GPa, 12.66 ±0.45 GPa, and 181.44 ±8.01 nm, respectively. In contrast, those of the pristine specimen are 0.68 ±0.04 GPa, 7.91 ±0.29 GPa, 8.65 ±0.34 GPa, and 236.67 ±11 nm, respectively. Thus, there was a significant increase in microhardness, Young's modulus, reduced modulus, and reduction in contact depth after

irradiation, as summarized in Figure 6. Considering that the average depth of the irradiated region calculated using SRIM was 623 nm, it can be stated that the 236.67 ± 11 nm deep indents recorded after irradiation were within the damaged irradiated region. Representative load versus penetration depth plots obtained from pristine and irradiated geopolymer using a load of 1 mN are presented in Figure 5(d). It is observed that there was a significant increase in the geopolymer hardness after irradiation, as shown in Table 2.

Table 2. Summary of statistical results of nanoindentation mechanical properties of pristine and irradiated metakaolin-based geopolymer.

Condition	Location Number	Distance from the center of the beam (μm)	Hardness (GPa)		Reduced Modulus (GPa)		Contact depth (nm)	
			Average	std.	Average	std.	Average	std.
Irradiated	1	0	1.13	0.75	12.22	4.43	197.4	66.6
	2	100	1.25	0.74	12.2	3.93	189.9	71.6
	3	200	1.32	0.76	12.87	4.65	178.2	55.8
	4	300	1.17	0.65	12.46	4.4	190.5	60.3
	5	400	1.29	0.86	12.55	5.13	183.9	58.6
	6	500	1.35	0.82	12.78	4.2	175.6	51.8
	7	600	1.28	0.71	12.83	4.22	178.4	51.3
	8	700	1.42	0.78	12.92	3.98	172	55.7
	9	800	1.34	0.71	12.85	4.21	176.3	58.8
	10	900	1.27	0.75	12.5	3.96	182.8	58.8
	11	1400	1.42	0.97	13.51	4.66	177.6	64.5
	12	1900	1.13	0.54	11.77	3.81	186.6	48.9
	13	2400	1.44	0.92	13.18	4.46	169.5	50.2
Pristine	1		0.64	0.29	8.3	2.45	249.1	63.2
	2		0.72	0.29	8.98	2.12	228.2	42.9
	3		0.68	0.24	8.68	1.83	232.7	42.8

The surface topography around the indents before and after irradiation was imaged by SEM to examine the topography of the indentation point and investigate the pile-up surrounding the indenter's tip. SEM images of the indentation point before and after irradiation are seen in Figure 7. The pyramidal tipped shape of the Berkovich diamond indenter imprint was not seen here for both the pristine and irradiated samples. This could have been due to the brittleness of the geopolymer, which resulted in the collapse of the geopolymer matrix underneath the tip of the indenter. Figures 7(a) and 7(b) exhibit pile-up morphology surrounding the indentation point in both pristine and irradiated samples. However, in the case of pristine, the pile-up is higher and more pronounced than in the irradiated situation due to the higher penetration depth reported for pristine (236.67 ± 11 nm) relative to irradiated (181.44 ± 8.01 nm) samples.

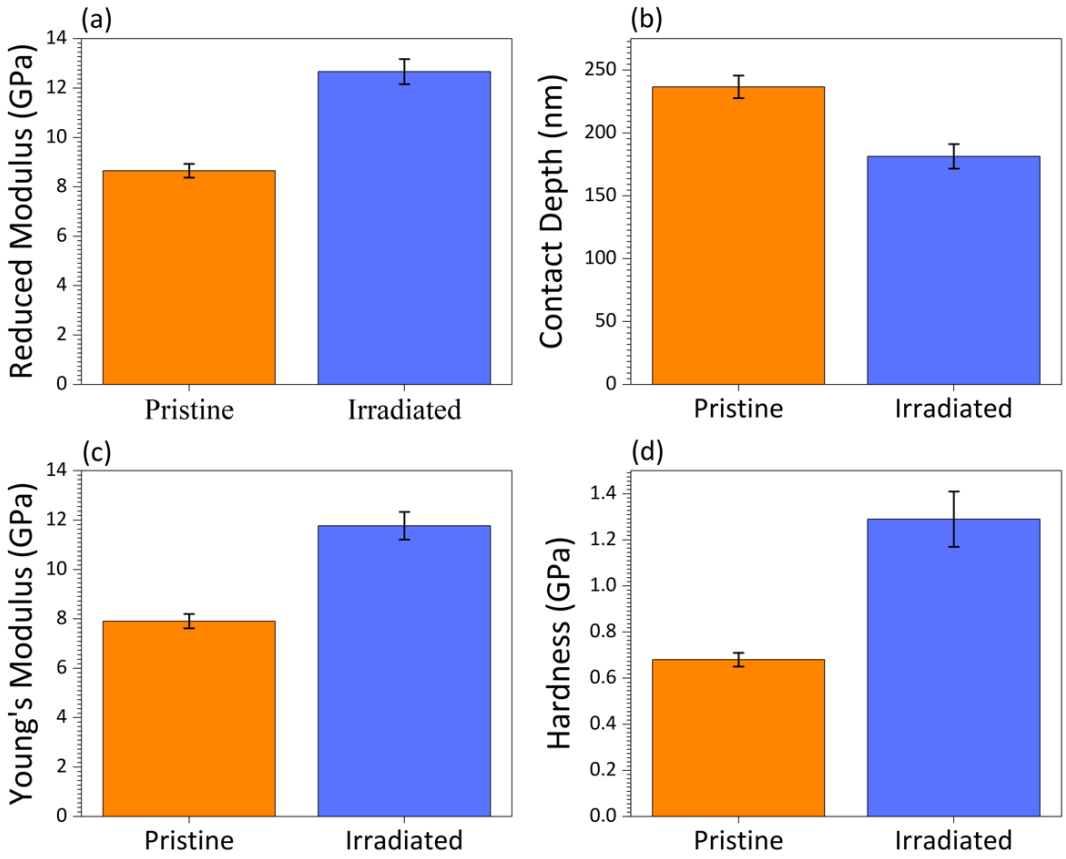

Figure 6. Average nanoindentation results of pristine and irradiated metakaolin-based geopolymer (a) reduced modulus, (b) contact depth, (c) Young's modulus, and (d) hardness.

Table 3. Summary of the average and standard deviation nanoindentation results, including hardness, Youngs's modulus, reduced modulus, and contact depth for pristine and irradiated metakaolin-based geopolymer.

Description		Average	Standard Deviation (std.)
Hardness (GPa)	Pristine	0.68	0.04
	Irradiated	1.29	0.10
Young's Modulus (GPa)	Pristine	7.91	0.29
	Irradiated	11.77	0.56
Reduced Modulus (GPa)	Pristine	8.65	0.34
	Irradiated	12.66	0.45
Contact depth (nm)	Pristine	236.67	11.00
	Irradiated	181.44	8.01

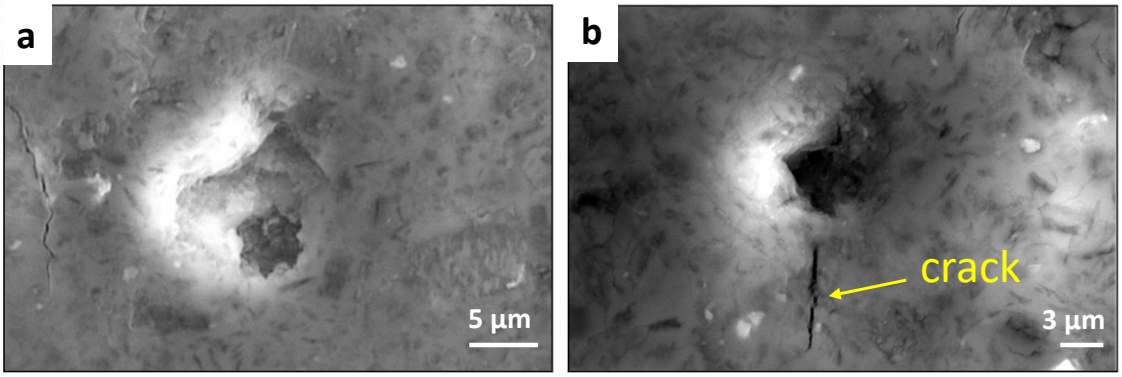

Figure 7. SEM images of indentation point: (a) indentation point for pristine sample and (b) indentation point for irradiated sample.

3.2 Chemical and Molecular Characterization

3.2.1 XRD Results

The diffraction patterns of metakaolin and pristine and irradiated geopolymer are plotted in Figure 8. Anatase (TiO_2) phase impurity was the primary phase observed in metakaolin and geopolymer, having diffraction maxima at 2θ of 25.3°, 27.39°, 37.81°, and 48.04°. The diffraction pattern and peak interpretation for anatase were consistent with (TiO_2, PDF number 04-013-3874) [41,42]. Also, a broad amorphous hump was observed in metakaolin and the pristine geopolymer at 2θ around 22° and 28°, respectively. Pristine and irradiated geopolymer showed a reduction in the anatase peak at [101] and [200] planes, which could be due to the geopolymerization process or the preferred crystal orientation. Moreover, XRD did not show any newly formed minerals after exposure to irradiation.

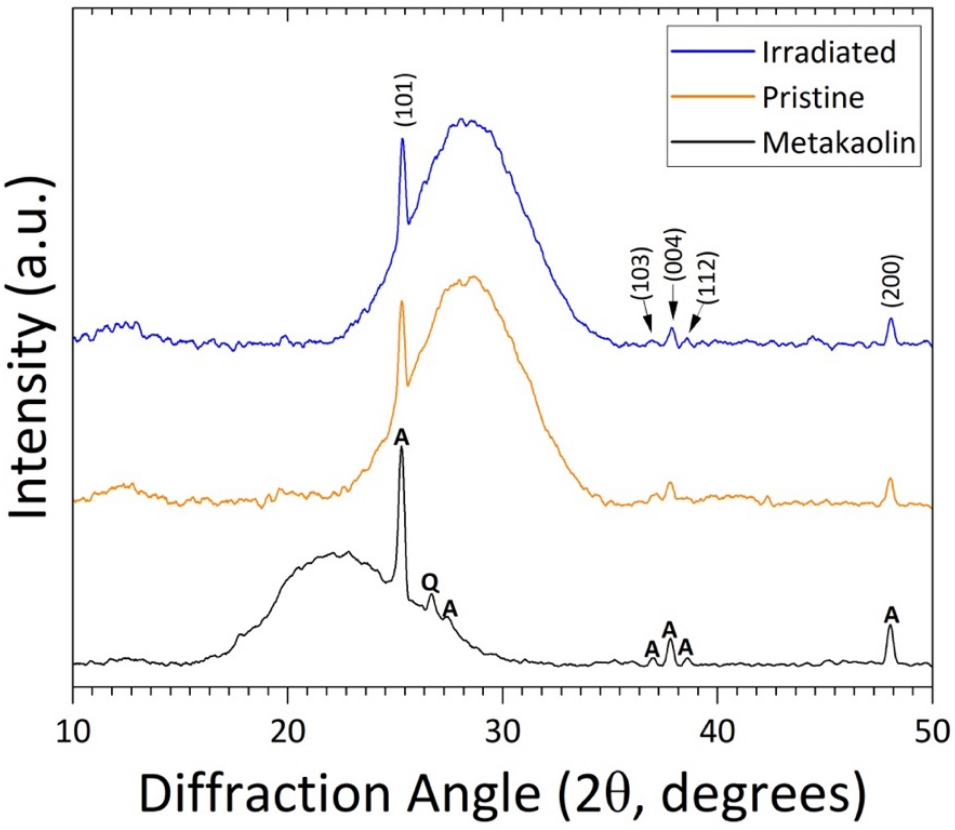

Figure 8. X-ray powder diffraction patterns resulting from metakaolin, pristine, and irradiated metakaolin-based geopolymer.

3.2.2 FTIR Results

Figure 9 presents the FTIR spectra of the pristine and irradiated geopolymer. Two absorption bands are observed in the pristine and irradiated samples within the wavenumber (WN) range of 3500-3300 cm^{-1} and 1639 cm^{-1}, which correspond to the O-H stretching vibration and H-O-H bending (blue and green regions, respectively) [43] or the deformation mode of coordinated water molecules adsorbed to the Si-O-Si structure [44,45]. Note that the peaks attributed to the H-O-H (H_2O band) and the O-H stretching vibration have decreased in intensity and exhibited peak broadening after exposure to irradiation. These changes are possible due to the difference in water content [46] resulting from the thermal effect of the ionization beam.

Moreover, the band around 1000 cm^{-1} (gray region) represents the asymmetric stretching band of Si-O-T (T is tetrahedral Si or Al) [47,48]. The peak at around 1436 cm^{-1} (orange region) represents the asymmetric stretching vibration mode of the O-C-O bond in the CO_3^{2-} group [47,49]. The presence of this peak is an indication that carbonation took place in the geopolymer gel [50]. After irradiation, the peak shifted towards the lower WN (1375 cm^{-1}) and became sharper and more well-defined.

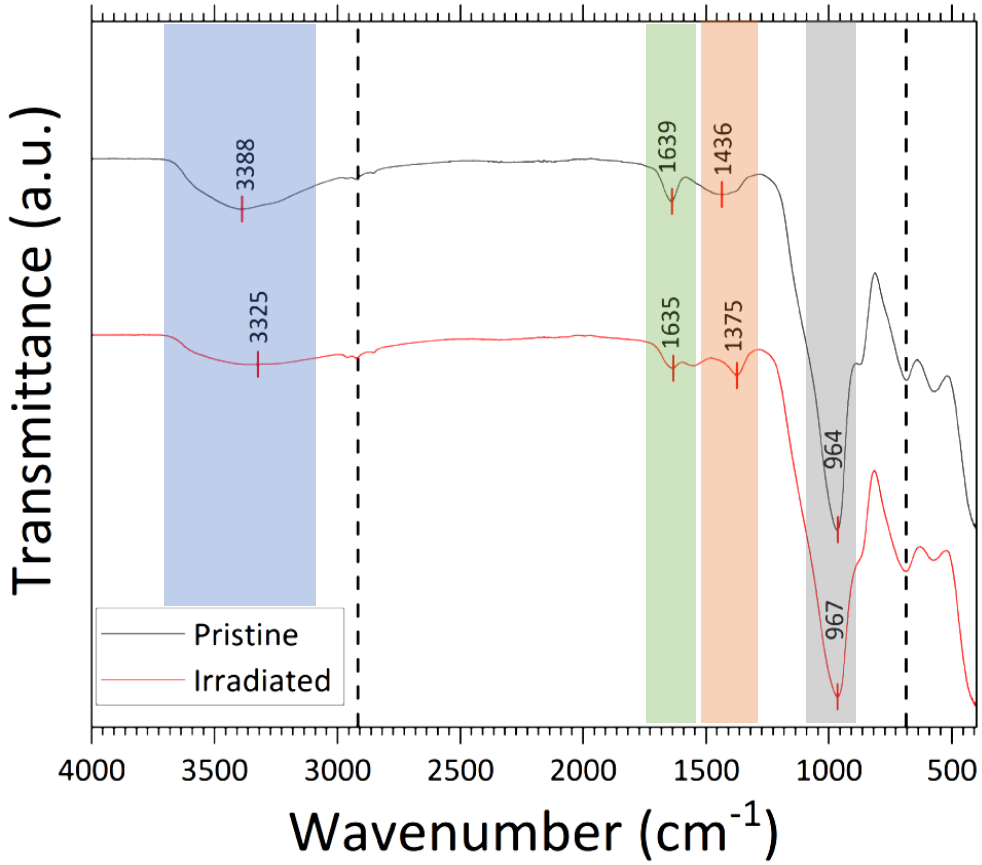

Figure 9. FTIR spectra of pristine versus irradiated metakaolin-based geopolymer in 4000–400 cm^{-1} wavenumber region, before and after the irradiation.

3.2.3 Raman Spectra Results

Figure 10 displays the Raman spectra of metakaolin and pristine and irradiated geopolymer. The results represent the data points collected over an area of 15 µm × 15 µm. Moreover, using a 532 nm excitation laser on irradiated samples yielded high fluorescence, and there were no peaks observed. This lack of peaks could be due to the presence of the titanium ion in the geopolymer matrix, which has the tendency to absorb the excitation laser and emit fluorescence that could interfere with the Raman scattering signal reflected from the geopolymer. However, using a 785 nm excitation laser eliminated the fluorescence effect from the Raman spectra. There were four major peaks located at 143 cm^{-1} (present in both metakaolin and pristine samples), 393 cm^{-1} (present in metakaolin) or 396 cm^{-1} (present in pristine), 518 cm^{-1} (present in metakaolin) or 516 cm^{-1} (present in pristine), and 638 cm^{-1} (present in both metakaolin and pristine samples). These peaks are attributed to intratetrahedral vibrations of polymerized [SiO_4] tetrahedral in quartz [50], bending modes of Si-O-Al and Si-O-Si, and a symmetric stretching mode of T-O (where T represents Si or Al) [51], respectively. However, Challagulla *et al.* [52] attributed similar Raman spectral modes to anatase TiO_2 and identified them as E_g, B_{1g}, A_{1g}, and E_g which correspond to 134, 382, 500, and 590 cm^{-1}, respectively. Similarly, Abdelrahman and Garg [42] reported that these four peaks correspond to the presence of anatase impurities in the metakaolin (raw materials), which they suggested that this is considered a drawback of using Raman spectroscopy as a characterization technique for metakaolin-based geopolymer.

(a)

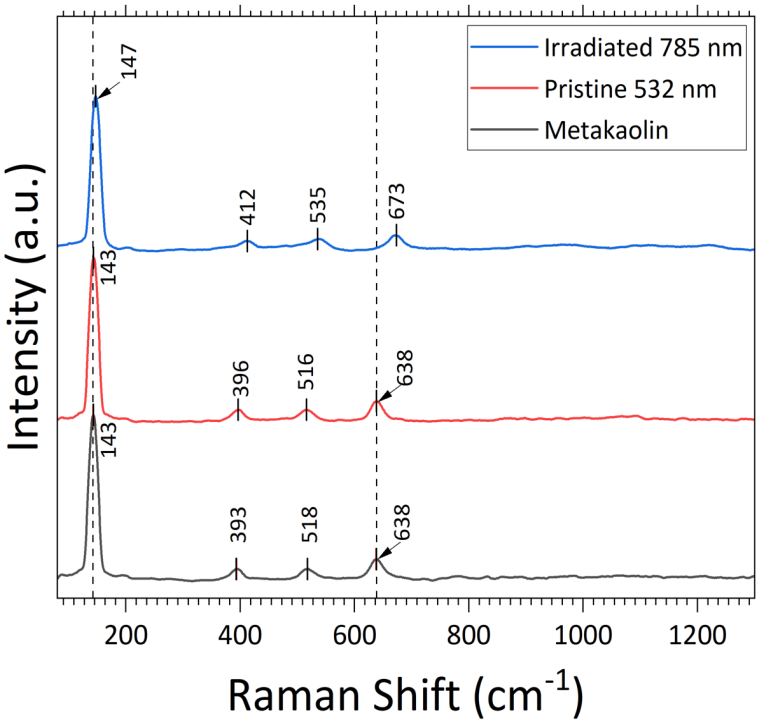

(b)

Condition	Peak Center cm^{-1}	FWHM
Irradiated	147	22
	412	183
	535	153
	673	697
Pristine	143	20
	393	226
	516	111
	638	51
Metakaolin	143	21
	393	158
	518	95
	638	131

Figure 10. Raman spectroscopy result from metakaolin powder, pristine, and irradiated metakaolin-based geopolymer a) Raman spectra of pristine and irradiated metakaolin-based geopolymer in 80–1300 cm^{-1} wavenumber region, before and after irradiation and b) a summary of calculated full width half maximum (FWHM) and location of the peak center.

Notably, there is no significant change in the position and intensity of these peaks between the metakaolin and geopolymer samples prior to irradiation. Also, there is a decrease in Raman intensity, a shift in peak position (to higher WN), and an increase in the peak full width half maximum (FWHM), as summarized in Figure 10(b). Generally, there is a major shift in all peaks after irradiation except for the peak seen at 143 cm^{-1} which has a slight shift to 147 cm^{-1} compared to other peaks.

4 Discussion

4.1 Microstructure and Morphology Analysis

4.1.1 Laser Profilometry

The results presented in Figure 2 indicate that irradiation has a significant impact on the surface morphology and structural integrity of the metakaolin-based geopolymer. The formation of the cracks at the geopolymer surface could be attributed to the energy produced from the Ti^{+} exposure. The conversion of this inelastic energy into thermal and mechanical energies results in the formation of a shockwave sufficient to cause atomic displacement within the bulk of the geopolymer structure [53,54]. The atomic displacement increased stress and strain at the geopolymer surface, which initiated the formation of the cracks and the modification of the surface in the form of a newly formed pore (Figure 2(b)). Moreover, the cracks were not only caused by the irradiation shock wave but also due to the intense heating followed by rapid cooling [53]. It should be noted that the radiation effect is confined to a very small area (beam diameter of 3 mm) near the surface, approximately within the first ~623 nm, as calculated using SRIM. Moreover, the exposure time (43 minutes) and the fluence (10^{16} cm^{-2}), as well as the high beam energy (526 keV Ti^{+} ion beam) used in our experiment, were considered extreme conditions for such a material. In addition, cracks in geopolymer formations may result not only from irradiation but also from the hydration and the volumetric strain that occurs due to water evaporation, surface energy, and hydrostatic tension [55]. Moreover, the line profiles presented in Figure 2(c) provide further insights into the surface changes induced by irradiation. Before irradiation, the geopolymer surface exhibited minimal alterations in roughness. In contrast, after irradiation, a significant drop in the line profile was observed, with a sharp peak at the location of the newly formed crack. This suggests that localized heating, thermal shock, and Ti+ deposition during irradiation lead to surface shrinkage caused by the evaporation of bound water. The combination of crack formation and surface shrinkage highlights the complexity of the material response under extreme irradiation conditions.

4.1.2 Scanning Electron Microscopy (SEM) and Backscattered Electron (BSE)

The SEM images (Figure 3) provided insights into the surface changes induced by irradiation. The experimental results suggest that the effect of irradiation was primarily confined to the immediate vicinity of the sample surface, as observed in both SEM and BSE images (Figure 3(f)). The shallow depth of the irradiation effect was further confirmed by the absence of discernible color differences between the pristine and irradiated areas in the BSE image. It was found that the irradiation-induced changes in the microstructure led to a significant reduction in surface porosity, resulting in a more uniform and compact microstructure. Comparing SEM and BSE images of pristine and irradiated samples (Figure 4), it was observed that irradiation resulted in the development of significant cracks, including an additional crack originating from a pre-existing one. The observed early crack formations in the geopolymer surface (Figure 3(a)) can be attributed to the material's low tensile strength behavior, akin to concrete. Such cracks can result from excessive tensile stress induced by restraint to early-age shrinkage and

drying shrinkage [56,57]. Similarly, Zatloukalova *et al.* [58] observed evenly distributed cracks on the surface of the cement paste samples before and after irradiation and concluded that these cracks were developed during the sample preparation for microstructure analysis. Thus, it is challenging to ascertain whether the cracks specifically arose due to irradiation or from a dehydration process resulting from atmospheric exposure.

Generally, geopolymers are known for their low thermal conductivity [46], which makes them excellent insulators [60–63]. In our experiment, thermal energy was trapped in the region exposed to radiation, leading to limited heat dissipation and subsequent shrinkage due to moisture evaporation. This phenomenon caused the irradiated section of the sample to appear darker than the pristine side (Figure 3(b)), indicating changes in surface topography resulting from irradiation-induced shrinkage. Additionally, variations in surface features, such as heights and slopes, can influence the angle of incidence and scattering of electrons [64]. Consequently, areas tilted away from the incident electron beam may receive fewer electrons and appear darker, while areas perpendicular to the beam may receive more electrons and appear brighter [64]. Figure 2 (c) provides visual confirmation of a depression on the sample surface after irradiation, as indicated by the line profile.

To assess the penetration depth of the irradiation effect, the backscattered electron (BSE) technique was employed. BSE possesses higher energy compared to secondary electrons, allowing them to be detected from greater depths within the specimen. This characteristic enables us to investigate the extent of the irradiation's impact beyond the surface of the sample [65]. Moreover, BSE signal intensity depends primarily on the average atomic number of the local area in the sample. The use of coupled detectors on both sides of the beam, along with flat polished sections, helps to eliminate topographical contrast [65]. In our analysis, we observed that unreacted metakaolin residuals, commonly present in the geopolymer microstructure due to improper mixing [66–68], were notably absent following irradiation. This phenomenon can be attributed to the temperature increase caused by Ti+ bombardment, as the energy from radiation is converted into heat [40]. Thus, irradiation contributed to an enhanced microstructure of the geopolymer surface, resulting in a significant reduction in surface porosity. These findings align with the study conducted by Sarker *et al.*[69] where they concluded that increasing the curing temperature leads to a denser microstructure in geopolymers. They attributed this increase in density to sintering and the enhancement of geopolymerization with higher temperatures. Therefore, enhancing the geopolymer surface by incorporating modifiers like fibers to mitigate surface cracks [70–73] would enhance the geopolymer's resilience against irradiation. These modifications could broaden the potential applications of geopolymers in various fields, including construction, where durability and radiation resistance are crucial factors to consider. Further research is warranted to explore the long-term behavior and performance of irradiated geopolymers, as well as to investigate tailored material modifications that optimize their properties for specific applications.

4.1.3 Nanoindentation

The obtained results presented in Figures 5(a), (b), and (c) display the contact depth, reduced modulus, and microhardness obtained from 13 different locations in the irradiated sample, starting from the center of the irradiated area and extending outward towards the pristine region (Figure 5e). The measurements were strategically conducted from the center of the irradiated area towards the pristine region of the sample to assess the effect of irradiation on the mechanical properties throughout the exposed area.

Interestingly, the nanoindentation results did not exhibit any specific trends in the contact depth, reduced modulus, or microhardness as a function of position from the center outward towards the pristine section of the sample. This lack of significant variations in mechanical properties suggests that the exposed area to radiation was uniformly affected by the irradiation process. However, it is worth noting that the reported results exhibited relatively high standard deviation values. This phenomenon can be attributed to the complex condition of the specimen after irradiation, where an inhomogeneous microstructure and surface modifications, including the formation of new cracks and an increase in surface roughness, may have contributed to the variability in the mechanical properties [74]. Nanoindentation on cement paste presents challenges due to the high heterogeneity of its surface, making it difficult to select specific material phases for indentation with sufficient repeatability [75]. In contrast, geopolymers offer an advantage in nanoindentation studies as they do not possess multiple phases, providing a more uniform and consistent surface for indentation analysis.

The average nanoindentation results obtained from the pristine and irradiated samples presented in Table 3 provided a clearer picture of the overall mechanical changes induced by irradiation. The irradiated geopolymer showed a significant increase in microhardness, Young's modulus, and reduced modulus, along with a reduction in contact depth compared to the pristine specimen. The enhanced microhardness and moduli after irradiation are consistent with the phenomenon of radiation hardening, commonly observed in materials exposed to ion bombardment [74,76–78]. This increase in hardness can be attributed to the formation of irradiation-induced defects, which act as obstacles, hindering the movement of dislocations and leading to improved mechanical properties [79,80]. The presence of anatase (TiO_2) phase impurity in both metakaolin and geopolymer samples is significant in understanding the mechanical behavior of the material. Although geopolymers are known to have an amorphous or semi-crystalline structure, the existence of TiO_2 crystals, even as impurities, may lead to the development of dislocations within the material upon exposure to ionizing radiation. The rise in microhardness observed after irradiation may be partially attributed to the deformation and strengthening effects of these impurity crystals. Moreover, the improvement in the microstructure following irradiation, as observed in the SEM and BSE images (Figure 3(d)), likely played a role in enhancing the mechanical properties of the irradiated geopolymer. The reduction in contact depth and increase in hardness further substantiate the influence of irradiation on the microstructure of the material.

The observed absence of a clear pyramidal shape in the indentation imprints shown in Figure 7 suggests that the geopolymer is highly brittle and prone to deformation under the applied load. The brittleness of the material could be attributed to its amorphous or semi-crystalline nature, which may limit the plastic deformation capacity and lead to collapse instead. As a result, the typical pyramid-shaped imprint characteristic of ductile materials was not evident in the geopolymer samples before and after irradiation. Despite the absence of a distinct pyramid shape, the presence of pile-up surrounding the indentation point indicates rigid-plastic deformation in the material [81] resulting from the dislocation glides together with microcracks initiation and propagation [82]. Pile-up occurs due to the flow of material around the indenter during the indentation process, and its extent can provide insights into the material's mechanical behavior. In the case of the pristine sample, the pile-up was higher and more pronounced compared to the irradiated sample. This difference can be attributed to the higher penetration depth recorded for the pristine sample (236.67 ± 11 nm) compared to the irradiated sample (181.44 ± 8.01 nm). The reduction in pile-up in the irradiated sample suggests that the material underwent less

plastic deformation or flow during the indentation process. This result aligns with the increase in microhardness observed after irradiation, indicating an enhancement in the material's hardness and resistance to plastic deformation. The changes in mechanical properties observed in the nanoindentation results are likely associated with alterations in the microstructure and bonding configurations induced by the ionizing radiation. The absence of pyramid-shaped imprints and the differences in pile-up morphology between the pristine and irradiated samples highlight the influence of irradiation on the mechanical behavior and deformation mechanisms of the geopolymer.

4.2 Chemical and Molecular Characterization

4.2.1 XRD

The X-ray diffraction (XRD) analysis of metakaolin, pristine geopolymer, and irradiated geopolymer samples, as presented in Figure 8, provides important findings into the crystalline phases and structural changes induced by irradiation. Geopolymers are known for their amorphous or semi-crystalline nature, which forms through the geopolymerization process involving alkali activators with aluminosilicate materials. Anatase (TiO_2) phase impurity was identified as the primary phase in both metakaolin and geopolymer samples. Additionally, the diffraction patterns exhibited a broad amorphous hump around 2θ angles of approximately 22° and 28° for metakaolin and the pristine geopolymer, respectively. This amorphous hump indicates the disordered or non-crystalline nature of the geopolymer structure. In XRD analysis, the intensity of peaks is directly related to the degree of crystallinity in the materials. For amorphous materials like geopolymers, with low crystallinity, broader and weaker peaks are typically observed. On the other hand, materials with well-ordered atomic arrangements, like the Anatase phase in our case, tend to produce sharp and intense peaks. Interestingly, upon irradiation, the XRD results demonstrated a reduction in the intensity of the anatase peaks at [101] and [200] planes in both the pristine and irradiated geopolymer samples. This decrease in peak intensity could be attributed to several factors, such as the geopolymerization process or changes in preferred crystal orientation induced by the ionizing radiation. The reduction in peak intensity suggests alterations in the crystallographic arrangement of the anatase phase in response to the irradiation exposure. Moreover, studies by Adjei *et al.* [83], have shown that heating metakaolin-based geopolymers to 73^{o} C led to the formation of gobbinsite and anorthite minerals within the geopolymer microstructure. This mineral formation during the thermal treatment introduces thermal stress into the material, which may potentially weaken the overall structure of the metakaolin-based geopolymer. From these findings revealed by Adjei *et al.* [83], we can infer that the temperature produced from the irradiation in our case didn't reach 73^{o} C and was not sufficient enough to form a new phase. Comparing these findings with the alterations observed in the anatase phase due to irradiation, it becomes apparent that different external stimuli such as heat or irradiation can influence the geopolymer structure in distinct ways.

Furthermore, the XRD analysis did not reveal the presence of any newly formed minerals or phases in the geopolymer samples after exposure to irradiation. This indicates that the irradiation process did not induce significant mineralogical changes or introduce new crystalline species in the material. The absence of newly formed minerals implies that the geopolymer matrix remains relatively stable under the conditions of the irradiation experiment. Further investigations into the mechanisms behind the observed changes in peak intensities and crystallographic arrangements would be of great interest in understanding the response of geopolymers to ionizing radiation and its potential implications for their performance in practical applications.

4.2.2 FTIR

The FTIR analysis offers crucial information about the molecular structure and chemical bonds of the geopolymer before and after irradiation. By examining the infrared spectra, we gain valuable information about the changes in vibrational modes and functional groups induced by ionizing radiation. The observed changes in the O-H stretching and H-O-H bending peaks after exposure to irradiation suggest alterations in water content due to the thermal effect of the ionization beam. In addition, it is known that high-energy neutrons can excite water molecules, leading to radiation-induced water decomposition (radiolysis) and subsequent drying due to gas release [8]. This phenomenon may also have an impact on the properties of geopolymer paste as they typically contain a significant amount of water in their composition. It is worth mentioning that cement paste exhibits similar behavior upon exposure to irradiation [8]. Moreover, Kontani *et al.* [84] highlight that gamma-ray irradiation readily decomposed the evaporable water in cement paste, while the chemically bound water remained mostly unaffected even under irradiation conditions. Additionally, the rates of hydrogen generation were influenced by both the dose rates of gamma-ray irradiation and the water content present in the cement paste specimens. In contrast, there is limited information available regarding the impact of neutrons on concrete materials, particularly on the water phases within cement paste. Neutrons, like gamma rays, excite water by transferring their energy to it. However, due to disparities in energy transfer density, neutrons may exhibit distinct effects on the microstructures of cement paste compared to gamma rays [84].

The absence of significant changes in the Si-O-T peak intensity suggests that no further geopolymeric linkages occurred upon irradiation. This indicates that the essential geopolymer structure remained relatively stable under the irradiation conditions. On the other hand, the shift and sharpening of the peak corresponding to the O-C-O bond in the CO_3^{2-} group suggests that carbonation took place in the geopolymer gel after irradiation [50]. The exact mechanism of this carbonation process requires further investigation. Overall, the FTIR analysis highlights the sensitivity of geopolymer materials to irradiation, particularly in terms of water content and carbonation. Understanding the effects of irradiation on the molecular structure of geopolymers is crucial for predicting their performance and potential applications in radiation-exposed environments.

4.2.3 Raman Spectra

The Raman spectroscopy results provide valuable insights into the molecular structure and vibrational characteristics of the geopolymer under irradiation. Initially, when using a 532 nm excitation laser on the irradiated samples, the Raman spectra showed high fluorescence and no distinct peaks were observed. The presence of the titanium ion in the geopolymer matrix likely contributed to this fluorescence behavior. Titanium ions have a propensity to absorb the excitation laser and emit fluorescence, which could interfere with the Raman scattering signal from the geopolymer. As a result, obtaining meaningful Raman spectra under these conditions proved challenging.

To address the fluorescence interference and enhance the clarity of the Raman spectra, a 785 nm excitation laser was utilized. This choice of excitation laser effectively eliminated the fluorescence effect from the Raman spectra, allowing for better resolution and identification of the characteristic peaks associated with the geopolymer's vibrational modes.

Prior to irradiation, the Raman spectra of both metakaolin and pristine geopolymer show no significant differences in peak position and intensity. This indicates that the geopolymerization process did not lead to substantial alterations in the molecular

structure compared to the raw metakaolin precursor. However, after irradiation, notable changes in the Raman spectra are observed. There is a decrease in Raman intensity, a shift in peak position (to higher wavenumbers), and an increase in the peak full-width half maximum (FWHM). These observations suggest that the irradiation has induced modifications in the molecular structure of the geopolymer. Interestingly, Li [85] identified the peak observed at 532 cm^{-1} as titanium ions in tetrahedral coordinate in TS-1 zeolite (titanium-silicalite molecular sieve). Li also stated that this peak appeared at a higher grafting temperature, which correlated with our case since we used Ti^{+} as an ionization source that introduced thermal shock to the material. We can assume that the titanium ions used in the experiment substituted within the silicate structure and formed a new bond which caused the peak to shift from $516\ cm^{-1}$ to $535\ cm^{-1}$. However, to prove this claim, another work needs to be done with metakaolin free of titanium oxide impurities. An increase in the FWHM of a Raman peak indicates that the vibrational mode associated with that peak was becoming broader and more disordered. This finding could be due to several factors, such as increased sample disorder (change of bond angles and bond distance [86]), sample heterogeneity, or an increase in the sample temperature [86]. An increase in FWHM can also indicate a decrease in the lifetime of the vibrational mode, which can be caused by factors such as an increase in the strength of the interactions between the molecules or a change in the local environment.

The Raman spectroscopy results provide compelling evidence of the structural changes occurring in the geopolymer following irradiation. The observed shifts in peak positions, changes in peak intensities, and broadening of certain peaks highlight the complex and dynamic nature of the geopolymer's response to ionizing radiation. These findings offer valuable insights into the irradiation-induced modifications in the molecular structure of the geopolymer and open up opportunities for further research to explore the implications of these changes on the material's properties, mechanical properties, and applications.

5 Conclusions and Future Scope

This paper investigated the effect of radiation on potassium metakaolin-based geopolymer paste using heavy Ti^{+} having an energy of 526 keV and fluence of 10^{16} cm^{-2} using an average beam current of 24 nA for 43 minutes of exposure duration. To study the effect of radiation on geopolymer, laser profilometry, SEM, and BSE techniques were used for the morphological and microstructural evaluation, combined with XRD, FTIR, and Raman spectroscopy for chemical and molecular investigation. Also, nanoindentation was used to study the microscale mechanical behavior of the geopolymers before and after irradiation. Our conclusions are as follows:

1) A laser profilometer revealed the formation of new cracks in the center and the corner of the irradiated area, which could be attributed to the exposure to Ti+ and localized heating accompanied by water loss and microcracking. The ion irradiation resulted in a shockwave with sufficient magnitude to cause atomic displacement within the bulk of the geopolymer structure.
2) SEM and BSE analysis verified the existence of newly formed cracks originating from pre-existing cracks within the geopolymer. However, it posed a challenge to definitively ascertain whether these cracks were solely induced by irradiation, or if they also resulted from the typical hydration process experienced by geopolymer due to moisture loss.

3) The geopolymer surface displayed a more homogenous and denser microstructure with the disappearance of the unreacted metakaolin powder after exposure to irradiation.
4) The results for hardness, Young's modulus, reduced modulus, and contact depth for the irradiated sample obtained from the nanoindentations were 1.29 $\pm$0.10 GPa, 11.77 $\pm$0.56 GPa, 12.66 $\pm$0.45 GPa, and 181.44 $\pm$8.01 nm, and for pristine specimen were 0.68 $\pm$0.04 GPa, 7.91 $\pm$0.29 GPa, 8.65 $\pm$0.34 GPa, and 236.67 $\pm$11 nm, respectively. These findings indicate an increase in hardness, Young's modulus, and reduced modulus, accompanied by a decrease in contact depth following irradiation. A notable rise in geopolymer hardness post-irradiation can be attributed to the interstitial substitution of Ti+ ions within the geopolymer structure and the observed enhancement in microstructure subsequent to irradiation.
5) XRD analysis indicated that the irradiation process did not result in the formation of any new minerals or phases in the geopolymer samples. The absence of significant mineralogical changes or the introduction of new crystalline species indicates that the irradiation had a limited impact on the material's mineral composition.
6) FTIR spectra after irradiation showed that the peaks attributed to O-H stretching vibration and H-O-H (H_2O band) have decreased intensity and exhibited peak broadening after exposure to irradiation, possibly due to the difference in water content resulting from the thermal effect of the ionization beam or due to the chemical reaction between Ti^+ and the geopolymer gel. The intensity of the Si-O-T peak did not show any change after irradiation, which suggested that no further geopolymeric linkages occurred due to the exposure to irradiation.
7) Raman spectroscopy revealed that there were no significant alterations in the position and intensity of the peaks between the metakaolin and geopolymer samples before irradiation. However, following irradiation, a decrease in Raman intensity, a shift in peak position towards higher wavenumbers, and an increase in the full width at half maximum (FWHM) of the peaks were observed.
8) This study shows that geopolymer has the potential to be used as a construction material in nuclear power plants. Thus, further research and development of geopolymer as a construction material in nuclear power plants is warranted.
9) The findings of this study provide valuable insights into the effects of irradiation on geopolymers, particularly regarding changes in microstructure, surface morphology, mineralogy, and mechanical properties. However, to fully understand the mechanisms driving these alterations and their long-term implications on the performance and durability of geopolymers in radiation-exposed conditions, further comprehensive studies are warranted.

Conflict of Interest

The authors declare that they have no conflict of interest.

Declaration of Generative AI and AI-assisted technologies in the writing process

During the preparation of this work, the authors used GPT-3.5 to improve readability and clarity. After using this tool, the authors reviewed and edited the content as needed and take full responsibility for the content of the publication.

Acknowledgments

This research was carried out in part in the Materials Research Laboratory (MRL) Central Research Facilities, University of Illinois at Urbana-Champaign (UIUC). The authors thank Dr. Timothy Spila from the MRL for his great help with the geopolymer irradiation step and Dr. Jessica Crystal Spear for performing the nanoindentation measurements. The authors also thank the staff scientists of the Microscopy Suite at the Beckman Institute for Advanced Science and Technology at UIUC, including Dr. T. Josek and Catherine Wallace, for their valuable assistance in SEM imaging. The work of Mahrous and Jasiuk was supported by the National Science Foundation Mechanics of Materials and Structures program (CMMI-1926353). The work of Trindade and Kriven was supported by the USACE ERDC CERL, under Contract Number USArmyW9132T-21-C-0005.

References

[1] K.G. Field, I. Remec, Y. Le Pape, Radiation effects in concrete for nuclear power plants - Part I: Quantification of radiation exposure and radiation effects, Nuclear Engineering and Design. 282 (2015) 126–143. https://doi.org/10.1016/j.nucengdes.2014.10.003

[2] R.G. Clark, Radiation damage to concrete, General Electric Co. Hanford Atomic Products Operation, Richland, Wash. (1958) No. HW-56195. https://www.osti.gov/biblio/4304779

[3] D.L. Fillmore, Literature review of the effects of radiation and temperature on the aging of concrete, (2004). https://doi.org/10.2172/910954.

[4] K.G. Field, I. Remec, Y. Le Pape, Radiation effects in concrete for nuclear power plants – Part I: Quantification of radiation exposure and radiation effects, Nuclear Engineering and Design. 282 (2015) 126–143. https://doi.org/10.1016/j.nucengdes.2014.10.003

[5] D.J. Naus, C.B. Oland, B.R. Ellingwood, C.J. Hookham, H.L. Graves, Summary and conclusions of a program addressing aging of nuclear power plant concrete structures, Nuclear Engineering and Design. 194 (1999) 73–96. https://doi.org/10.1016/s0029-5493(99)00170-3

[6] P.A. Rasheed, S.K. Nayar, I. Barsoum, A. Alfantazi, Degradation of concrete structures in nuclear power plants: a review of the major causes and possible preventive measures, Energies 2022, Vol. 15, Page 8011. 15 (2022) 8011. https://doi.org/10.3390/en15218011.

[7] Z.P. Bazant, A. Steffens, Mathematical model for kinetics of alkali–silica reaction in concrete, Cement and concrete research. 30 (2000) 419–428. https://doi.org/10.1016/s0008-8846(99)00270-7.

[8] Y Khmurovska and P Štemberk 2019 IOP Conf. Ser.: Mater. Sci. Eng. 596 012035. https://doi.org/10.1088/1757-899x/596/1/012035

[9] T.M. Rosseel, I. Maruyama, Y. Le Pape, O. Kontani, A.B. Giorla, I. Remec, J.J. Wall, M. Sircar, C. Andrade, M. Ordonez, Review of the current state of knowledge on the effects of radiation on concrete, Journal of Advanced Concrete Technology. 14 (2016) 368–383. https://doi.org/10.3151/jact.14.368.

[10] M. Yang, S.R. Paudel, E. Asa, Comparison of pore structure in alkali activated fly ash geopolymer and ordinary concrete due to alkali-silica reaction using micro-computed tomography, Constr Build Mater. 236 (2020). https://doi.org/10.1016/j.conbuildmat.2019.117524

[11] J. Davidovits, Geopolymers: Inorganic polymeric new materials, Journal of Thermal Analysis and calorimetry. 37 (2005) 1633–1656. https://doi.org/10.1007/bf01912193.

[12] W.M. Kriven, Geopolymers and geopolymer-derived composites, Encyclopedia of Materials: Technical Ceramics and Glasses. 1–3 (2021) 424–438. https://doi.org/10.1016/b978-0-12-818542-1.00100-4

[13] W.M. Kriven, Geopolymer-based composites, Comprehensive Composite Materials II. (2018) 269–280. https://doi.org/10.1016/b978-0-12-803581-8.09995-1.

[14] K. Ramujee, M. Potharaju, Mechanical properties of geopolymer concrete composites, Mater Today Proc. 4 (2017) 2937–2945. https://doi.org/10.1016/j.matpr.2017.02.175

[15] K. Korniejenko, E. Frączek, E. Pytlak, M. Adamski, Mechanical properties of geopolymer composites reinforced with natural fibers, Procedia Eng. 151 (2016) 388–393. https://doi.org/10.1016/j.proeng.2016.07.395

[16] T. Wang, X. Fan, C. Gao, C. Qu, J. Liu, G. Yu, The influence of fiber on the mechanical properties of geopolymer concrete: A review, Polymers (Basel). 15 (2023). https://doi.org/10.3390/polym15040827

[17] P. Duxson, J.L. Provis, G.C. Lukey, S.W. Mallicoat, W.M. Kriven, J.S.J. Van Deventer, Understanding the relationship between geopolymer composition, microstructure and mechanical properties, Colloids Surf A Physicochem Eng Asp. 269 (2005) 47–58. https://doi.org/10.1016/j.colsurfa.2005.06.060

[18] M. Lahoti, K.H. Tan, E.H. Yang, A critical review of geopolymer properties for structural fire-resistance applications, Constr Build Mater. 221 (2019) 514–526. https://doi.org/10.1016/j.conbuildmat.2019.06.076

[19] J. Davidovits, geopolymer cement, (2013). www.geopolymer.org (accessed March 17, 2023).

[20] W.G. Valencia Saavedra, R. Mejía de Gutiérrez, Performance of geopolymer concrete composed of fly ash after exposure to elevated temperatures, Constr Build Mater. 154 (2017) 229–235. https://doi.org/10.1016/j.conbuildmat.2017.07.208

[21] M. Amran, S.S. Huang, S. Debbarma, R.S.M. Rashid, Fire resistance of geopolymer concrete: A critical review, Constr Build Mater. 324 (2022). https://doi.org/10.1016/j.conbuildmat.2022.126722

[22] B. Kim, J. Kang, Y. Shin, T. min Yeo, W. Um, Immobilization mechanism of radioactive borate waste in phosphate-based geopolymer waste forms, Cem Concr Res. 161 (2022) 106959. https://doi.org/10.1016/j.cemconres.2022.106959

[23] L. Zheng, W. Wang, Y. Shi, The effects of alkaline dosage and Si/Al ratio on the immobilization of heavy metals in municipal solid waste incineration fly ash-based geopolymer, Chemosphere. 79 (2010) 665–671. https://doi.org/10.1016/j.chemosphere.2010.02.018

[24] Q. Li, Z. Sun, D. Tao, Y. Xu, P. Li, H. Cui, J. Zhai, Immobilization of simulated radionuclide 133Cs+ by fly ash-based geopolymer, J Hazard Mater. 262 (2013) 325–331. https://doi.org/10.1016/j.jhazmat.2013.08.049

[25] H.N. Hamzah, M.M. Al Bakri Abdullah, H.C. Yong, M.R.R.A. Zainol, K. Hussin, Review of soil stabilization techniques: Geopolymerization method one of the new technique, Key Eng Mater. 660 (2015) 298–304. https://doi.org/10.4028/www.scientific.net/kem.660.298

[26] M.A. Mahrous, B. Šegvić, G. Zanoni, S.D. Khadka, S. Senadheera, P.W. Jayawickrama, The role of clay swelling and mineral neoformation in the stabilization of high plasticity soils treated with the fly ash-and metakaolin-based geopolymers, Minerals 2018, Vol. 8, Page 146. 8 (2018) 146. https://doi.org/10.3390/min8040146.

[27] S. Petlitckaia, Y. Barré, T. Piallat, O. Grauby, D. Ferry, A. Poulesquen, Functionalized geopolymer foams for cesium removal from liquid nuclear waste, J Clean Prod. 269 (2020). https://doi.org/10.1016/j.jclepro.2020.122400.

[28] D.S. Perera, E.R. Vance, Z. Aly, J. Davis, C.L. Nicholson, Immobilization of Cs and Sr in geopolymers with Si/Al Molar Ratio of~2, Ceramic Transactions. 176 (2006) 91–96. https://doi.org/10.1002/9781118407950.ch10

[29] Z. Yunsheng, S. Wei, C. Qianli, C. Lin, Synthesis and heavy metal immobilization behaviors of slag based geopolymer, J Hazard Mater. 143 (2007) 206–213. https://doi.org/10.1016/j.jhazmat.2006.09.033

[30] X. Liu, Y. Ding, X. Lu, Immobilization of simulated radionuclide 90Sr by fly ash-slag-metakaolin–based geopolymer, Http://Dx.Doi.Org/10.1080/00295450.2017.1292810. 198 (2017) 64–69. https://doi.org/10.1080/00295450.2017.1292810

[31] D. Lambertin, C. Boher, A. Dannoux-Papin, K. Galliez, A. Rooses, F. Frizon, Influence of gamma ray irradiation on metakaolin based sodium geopolymer, Journal of Nuclear Materials. 443 (2013) 311–315. https://doi.org/10.1016/j.jnucmat.2013.06.044

[32] N. Deng, H. An, H. Cui, Y. Pan, B. Wang, L. Mao, J. Zhai, Effects of gamma-ray irradiation on leaching of simulated 133Cs+ radionuclides from geopolymer wasteforms, Journal of Nuclear Materials. 459 (2015) 270–275. https://doi.org/10.1016/j.jnucmat.2015.01.052

[33] S.S. Musil, W.M. Kriven, In situ mechanical properties of chamotte particulate reinforced, Potassium Geopolymer, Journal of the American Ceramic Society. 97 (2014) 907–915. https://doi.org/10.1111/jace.12736.

[34] K.G. Field, I. Remec, Y. le Pape, Radiation effects in concrete for nuclear power plants – Part I: Quantification of radiation exposure and radiation effects, Nuclear Engineering and Design. 282 (2015) 126–143. https://doi.org/10.1016/j.nucengdes.2014.10.003

[35] M.L. Swanson, J.R. Parsons, C.W. Hoelke, Damaged regions in neutron-irradiated and ion-bombarded Ge and Si, https://doi.org/10.1080/00337577108231056

[36] J.F. Ziegler, M.D. Ziegler, J.P. Biersack, SRIM - The stopping and range of ions in matter (2010), Nucl Instrum Methods Phys Res B. 268 (2010). https://doi.org/10.1016/j.nimb.2010.02.091

[37] D. Nečas, P. Klapetek, Gwyddion: An open-source software for SPM data analysis, Central European Journal of Physics. 10 (2012) 181–188. https://doi.org/10.2478/s11534-011-0096-2/metrics

[38] J. Hay, Introduction to instrumented indentation testing, Experimental techniques, (2009). https://doi.org/10.1111/j.1747-1567.2009.00541.x.

[39] S. Chen, C. Wu, D. Yan, Binder-scale creep behavior of metakaolin-based geopolymer, Cem Concr Res. 124 (2019) 105810. https://doi.org/10.1016/j.cemconres.2019.105810

[40] Hilsdorf, H. K., Kropp, J., & Koch, H. (1978). The Effects of Nuclear Radiation on the Mechanical Properties of Concrete. Special Publication, 55, 223–254. https://doi.org/10.14359/6616

[41] C.J. Howard, T.M. Sabine, F. Dickson, Structural and thermal parameters for rutile and anatase, Acta Crystallographica Section B. 47 (1991) 462–468. https://doi.org/10.1107/s010876819100335x

[42] O. Abdelrahman, N. Garg, Impact of Na/Al ratio on the extent of alkali-activation reaction: non-linearity and diminishing returns, Front Chem. 9 (2022) 1181. https://doi.org/10.3389/fchem.2021.806532/bibtex.

[43] M. Stein, A. Georgiadis, D. Gudat, T. Rennert, Formation and properties of inorganic Si-contaminant compounds, Environmental Pollution. 265 (2020) 115032. https://doi.org/10.1016/J.ENVPOL.2020.115032.

[44] R. Ellerbrock, M. Stein, J. Schaller, Comparing amorphous silica, short-range-ordered silicates and silicic acid species by FTIR, Scientific Reports 2022 12:1. 12 (2022) 1–8. https://doi.org/10.1038/s41598-022-15882-4

[45] S. Mabroum, Y. Taha, M. Benzaazoua, R. Hakkou, Recycling of marls from phosphate by-products to produce alkali-activated geopolymers, Mater Today Proc. 51 (2021) 1931–1936. https://doi.org/10.1016/j.matpr.2021.03.206

[46] R. Kizil, J. Irudayaraj, K. Seetharaman, Characterization of irradiated starches by using FT-Raman and FTIR spectroscopy, Journal of agricultural and food chemistry, 50, no. 14 (2002) 3912-3918. https://doi.org/10.1021/jf011652p.

[47] Q. Wan, F. Rao, S. Song, R.E. García, R.M. Estrella, C.L. Patiño, Y. Zhang, Geopolymerization reaction, microstructure and simulation of metakaolin-based geopolymers at extended Si/Al ratios, Cem Concr Compos. 79 (2017) 45–52. https://doi.org/10.1016/j.cemconcomp.2017.01.014

[48] A. Hajimohammadi, J.L. Provis, J.S.J. Van Deventer, Effect of alumina release rate on the mechanism of geopolymer gel formation, Chemistry of Materials. 22 (2010) 5199–5208. https://doi.org/10.1021/cm101151n/asset/images/large/cm-2010-01151n_0008.jpeg

[49] K. Chen, W.T. Lin, W. Liu, Effect of NaOH concentration on properties and microstructure of a novel reactive ultra-fine fly ash geopolymer, Advanced Powder Technology. 32 (2021) 2929–2939. https://doi.org/10.1016/j.apt.2021.06.008

[50] K. Brylewska, P. Rożek, M. Król, W. Mozgawa, The influence of dealumination/desilication on structural properties of metakaolin-based geopolymers, Ceramics International, 44 (2018) 12853–12861. https://doi.org/10.1016/j.ceramint.2018.04.095.

[51] L. Zhang, F. Zhang, M. Liu, X. Hu, Novel sustainable geopolymer based syntactic foams: An eco-friendly alternative to polymer based syntactic foams, Chemical Engineering Journal. 313 (2017) 74–82. https://doi.org/10.1016/j.cej.2016.12.046

[52] S. Challagulla, K. Tarafder, R. Ganesan, S. Roy, Structure sensitive photocatalytic reduction of nitroarenes over TiO_2, Scientific Reports 2017 7:1. 7 (2017) 1–11. https://doi.org/10.1038/s41598-017-08599-2

[53] K.S. Jheeta, D.C. Jain, Ravi Kumar, K.B. Garg, Effect of titanium ion irradiation on the surface and defect centre formation in sapphire, Solid State Commun. 144 (2007) 460–465. https://doi.org/10.1016/j.ssc.2007.09.013

[54] V.A. Skuratov, S.J. Zinkle, A.E. Efimov, K. Havancsak, Swift heavy ion-induced modification of Al_2O_3 and MgO surfaces, Nucl Instrum Methods Phys Res B. 203 (2003) 136–140. https://doi.org/10.1016/s0168-583x(02)02197-3

[55] B. Rath, Effect of natural rubber latex on the shrinkage behavior and porosity of geopolymer concrete, Structural Concrete. 23 (2022) 2150–2161. https://doi.org/10.1002/suco.202000788

[56] I. Khan, T. Xu, A. Castel, R.I. Gilbert, M. Babaee, Risk of early age cracking in geopolymer concrete due to restrained shrinkage, Constr Build Mater. 229 (2019) 116840. https://doi.org/10.1016/j.conbuildmat.2019.116840

[57] Q.J. Frayyeh, M.H. Kamil, The effect of adding fibers on dry shrinkage of geopolymer concrete, Civil Engineering Journal. 7 (2021) 2099–2108. https://doi.org/10.28991/cej-2021-03091780

[58] J. Zatloukalová, V. Dewynter-Marty, J. Zatloukal, K. Kolář, F. Bernachy-Barbe, P. Bezdička, P. Konvalinka, Microstructural and micro-mechanical property changes of cement pastes for ILW immobilization due to irradiation, Journal of Nuclear Materials. 540 (2020) 152346. https://doi.org/10.1016/j.jnucmat.2020.152346

[59] Y. Huang, L. Gong, Y. Pan, C. Li, T. Zhou, X. Cheng, Facile construction of the aerogel/geopolymer composite with ultra-low thermal conductivity and high mechanical performance, RSC Adv. 8 (2018) 2350–2356. https://doi.org/10.1039/c7ra12041a

[60] E. Ul Haq, S. Kunjalukkal Padmanabhan, A. Licciulli, Microwave synthesis of thermal insulating foams from coal derived bottom ash, Fuel Processing Technology. 130 (2015) 263–267. https://doi.org/10.1016/j.fuproc.2014.10.017

[61] J. Henon, A. Alzina, J. Absi, D.S. Smith, S. Rossignol, Potassium geopolymer foams made with silica fume pore forming agent for thermal insulation, Journal of Porous Materials. 20 (2013) 37–46. https://doi.org/10.1007/s10934-012-9572-3/figures/9

[62] V. Vaou, D. Panias, Thermal insulating foamy geopolymers from perlite, Miner Eng. 23 (2010) 1146–1151. https://doi.org/10.1016/j.mineng.2010.07.015

[63] J. Feng, R. Zhang, L. Gong, Y. Li, W. Cao, X. Cheng, Development of porous fly ash-based geopolymer with low thermal conductivity, Materials & Design (1980-2015). 65 (2015) 529–533. https://doi.org/10.1016/j.matdes.2014.09.024

[64] J.I. Goldstein, D.E. Newbury, P. Echlin, D.C. Joy, C.E. Lyman, E. Lifshin, L. Sawyer, J.R. Michael, Scanning Electron Microscopy and X-ray Microanalysis, (2003). https://doi.org/10.1007/978-1-4615-0215-9

[65] K.L. Scrivener, Backscattered electron imaging of cementitious microstructures: understanding and quantification, Cem Concr Compos. 26 (2004) 935–945. https://doi.org/10.1016/j.cemconcomp.2004.02.029

[66] Y. Lu, N. Cui, Y. Xian, J. Liu, C. Xing, N. Xie, D. Wang, Microstructure Evolution Mechanism of Geopolymers with Exposure to High-Temperature Environment, Crystals 2021, Vol. 11, Page 1062. 11 (2021) 1062. https://doi.org/10.3390/cryst11091062.

[67] H.K. Tchakouté, C.H. Rüscher, S. Kong, E. Kamseu, C. Leonelli, Comparison of metakaolin-based geopolymer cements from commercial sodium waterglass and sodium waterglass from rice husk ash, J Solgel Sci Technol. 78 (2016) 492–506. https://doi.org/10.1007/s10971-016-3983-6/figures/14

[68] M.S. Muñiz-Villarreal, A. Manzano-Ramírez, S. Sampieri-Bulbarela, J.R. Gasca-Tirado, J.L. Reyes-Araiza, J.C. Rubio-Ávalos, J.J. Pérez-Bueno, L.M. Apatiga, A. Zaldivar-Cadena, V. Amigó-Borrás, The effect of temperature on the geopolymerization process of a metakaolin-based geopolymer, Mater Lett. 65 (2011) 995–998. https://doi.org/10.1016/j.matlet.2010.12.049.

[69] P.K. Sarker, S. Kelly, Z. Yao, Effect of fire exposure on cracking, spalling and residual strength of fly ash geopolymer concrete, Mater Des. 63 (2014) 584–592. https://doi.org/10.1016/j.matdes.2014.06.059

[70] P.F. Keane, J.S. Foltz, V. Chadha, C.P. Marsh, W.M. Kriven, Amorphous self-healed, chopped basalt fiber-reinforced, geopolymer composites, Journal of the American Ceramic Society. 104 (2021) 3443–3451. https://doi.org/10.1111/jace.17648

[71] A.C.C. Trindade, F. de Andrade Silva, W.M. Kriven, Mechanical behavior of K-geopolymers reinforced with silane-coated basalt fibers, Journal of the American Ceramic Society. 104 (2021) 437–447. https://doi.org/10.1111/jace.17446

[72] K. Sankar, A.C. Constâncio Trindade, W.M. Kriven, The influence of alkaline treatment on the mechanical performance of geopolymer composites reinforced with Brazilian malva and curaua fibers, Journal of the American Ceramic Society. 106 (2023) 339–353. https://doi.org/10.1111/jace.18716

[73] L. Li, H.X. Sun, Y. Zhang, B. Yu, Surface cracking and fractal characteristics of bending fractured polypropylene fiber-reinforced geopolymer mortar, Fractal and Fractional 2021, Vol. 5, Page 142. 5 (2021) 142. https://doi.org/10.3390/fractalfract5040142.

[74] C. Liu, C. Yu, N. Hashimoto, S. Ohnuki, M. Ando, K. Shiba, S. Jitsukawa, Micro-structure and micro-hardness of ODS steels after ion irradiation, Journal of Nuclear Materials, 2011. https://doi.org/10.1016/j.jnucmat.2011.01.067.

[75] M. Miller, C. Bobko, M. Vandamme, F.J. Ulm, Surface roughness criteria for cement paste nanoindentation, Cem Concr Res. 38 (2008) 467–476. https://doi.org/10.1016/J.CEMCONRES.2007.11.014.

[76] H. Sattar, S. Jielin, H. Ran, M. Imran, W. Ding, P. Das Gupta, H. Ding, Impact of microstructural properties on hardness of tungsten heavy alloy evaluated by stand-off LIBS after PSI plasma irradiation, Journal of Nuclear Materials. 540 (2020). https://doi.org/10.1016/j.jnucmat.2020.152389

[77] R. Kögler, W. Anwand, A. Richter, M. Butterling, X. Ou, A. Wagner, C.L. Chen, Nanocavity formation and hardness increase by dual ion beam irradiation of oxide dispersion strengthened FeCrAl alloy, Journal of Nuclear Materials. 427 (2012). https://doi.org/10.1016/j.jnucmat.2012.04.029

[78] C. Fu, J. Li, J. Bai, Y. Li, Q. Chen, G. Lei, J. Lin, Z. Zhu, Y. Meng, Effect of helium bubbles on irradiation hardening of additive manufacturing 316L stainless steel under high temperature He ions irradiation, Journal of Nuclear Materials. 550 (2021). https://doi.org/10.1016/j.jnucmat.2021.152948

[79] S.J. Zinkle, G.S. Was, Materials challenges in nuclear energy, Acta Mater. 61 (2013) 735–758. https://doi.org/10.1016/j.actamat.2012.11.004

[80] H.F. Huang, J.J. Li, D.H. Li, R.D. Liu, G.H. Lei, Q. Huang, L. Yan, TEM, XRD and nanoindentation characterization of Xenon ion irradiation damage in austenitic stainless steels, Journal of Nuclear Materials. 454 (2014) 168–172. https://doi.org/10.1016/j.jnucmat.2014.07.033

[81] J. Hu, Y. Zhang, W. Sun, T. Zhang, Nanoindentation-Induced Pile-Up in the Residual Impression of Crystalline Cu with Different Grain Size, Crystals 2018, Vol. 8, Page 9. 8 (2017) 9. https://doi.org/10.3390/CRYST8010009.

[82] Z.T. Wu, Z.B. Qi, D.F. Zhang, Z.C. Wang, Nanoindentation induced plastic deformation in nanocrystalline ZrN coating, Mater Lett. 164 (2016) 120–123. https://doi.org/10.1016/J.MATLET.2015.10.091.

[83] S. Adjei, S. Elkatatny, K. Ayranci, Effect of Elevated Temperature on the Microstructure of Metakaolin-Based Geopolymer, ACS Omega. 7 (2022) 10268–10276. https://doi.org/10.1021/ACSOMEGA.1C06878/ASSET/IMAGES/LARGE/AO1C06878_0012.JPEG.

[84] O. Kontani, S. Sawada, I. Maruyama, M. Takizawa, O. Sato, Evaluation of Irradiation Effects on Concrete Structure: Gamma-Ray Irradiation Tests on Cement Paste,

American Society of Mechanical Engineers, Power Division (publication) power. 2 (2014). https://doi.org/10.1115/power2013-98099

[85] C. Li, Identifying the isolated transition metal ions/oxides in molecular sieves and on oxide supports by UV resonance Raman spectroscopy, J Catal. 216 (2003) 203–212. https://doi.org/10.1016/s0021-9517(02)00107-0

[86] J. You, G. Jiang, K. Xu, High temperature Raman spectra of sodium disilicate crystal, glass and its liquid, J Non Cryst Solids. 282 (2001) 125–131. https://doi.org/10.1016/s0022-3093(01)00335-0